A theory of cloud spacing for equilibrium deep convection

Hao Fu* and Morgan O'Neill
Department of Earth System Science, Stanford University

* email: haofu736@gmail.com

This is a preprint for EarthArXiv. The manuscript has been submitted to *Journal of the Atmospheric Sciences*. Subsequent versions may have slight modifications. The authors welcome feedbacks from anyone who reads the manuscript.

A theory of cloud spacing for equilibrium deep convection

Hao Fu,[a] Morgan O'Neill,[a]

[a] *Department of Earth System Science, Stanford University, California*

Corresponding author: Hao Fu, haofu736@gmail.com

ABSTRACT: Precipitating convection is an important component of tropical atmospheric circulation. A cloud typically persists for an hour before it is shut down by its own evaporation-driven downdraft, which generates a gust front in the mixed layer that triggers neighboring clouds. There is no systematic theory for what sets the spacing of precipitating clouds, which is the first step towards understanding cloud interaction. We propose to view precipitating convection as a piecewise linear oscillator with cutoff, which separately describes the physical processes in the convective and recovery phase, but considers the stabilizing and destabilizing effects in a holistic way. The first hypothesis is that the cloud spacing is determined by the optimal (most unstable) mode of this system. Too short a spacing does not allow the gust front moisture to recover sufficiently, and too long a spacing makes the gust front's dynamical lifting effect too weak. The second hypothesis is that the optimal mode should be neutral to convection in equilibrium. Further analysis shows that the destabilizing effect of the gust front's triggering should be balanced by the damping effect of incomplete recovery and cold pool entrainment. This leads to a theory of cloud spacing for equilibrium deep convection, which predicts an upper bound that is proportional to the inverse of the cold pool fractional entrainment rate. The theory is benchmarked against a series of large-eddy simulations. The increase and stagnancy of cloud spacing with increased rain evaporation rate are well predicted by the theory.

1. Introduction

Individual deep convection is an important component of the tropical circulation (Emanuel 1994). It typically has a radius of a few kilometers and dies in an hour due to the precipitation-driven downdraft induced by the buoyant updraft. The evaporation of raindrops leads to a pool of cold air (cold pool), which spreads in the mixed layer. The gust front can accumulate and lift the boundary layer moist and buoyant air to the level of free convection, and trigger future convection, completing a convective life-cycle (Tompkins 2001; Grandpeix and Lafore 2010; Langhans and Romps 2015; Torri et al. 2015; Fuglestvedt and Haerter 2020). The clouds are strongly coupled to each other by the cold pool, at least in the tens-of-kilometers range (Feng et al. 2015; Haerter et al. 2019). There are still many puzzles about the role of cold pools in cloud interaction. For example, one ongoing debate is whether cold pools suppress or favor convective self-aggregation (CSA), which refers to the spontaneous formation of cloud clusters in a doubly periodic domain simulation over uniform sea surface temperature (Wing et al. 2017; Jeevanjee and Romps 2013; Haerter et al. 2019; Nissen and Haerter 2021; Yang et al. 2021).

To understand the complicated cloud interaction mechanism, a starting point is to study the convective life-cycle and spacing in an equilibrium state, over a sea surface of uniform temperature and without vertical wind shear. The maximum cold pool size, which is defined as the gust front travel distance that makes its buoyancy fully recover to the environmental value, has been analytically studied by Romps and Jeevanjee (2016). They considered the cold pool to be dissipated by surface heating and entraining the environmental air, and found that the maximum size increases with the initial cold pool volume and buoyancy anomaly. However, previous works have shown with simulations that cold pools collide with each other when they are still active and could trigger new convection with the residual momentum (Tompkins 2001; Torri and Kuang 2019). Nissen and Haerter (2021) found that the cold pool size distribution in a simulation has a minimal and maximal value, which indicates the existence of a characteristic cold pool size in equilibrium deep convection. The relationship between the equilibrium cold pool size (or equivalently the cloud spacing) and the maximum cold pool size remains unclear. There is evidence that the cloud spacing is highly variable. Gentine et al. (2016) found in simulations that cold pools are smaller when the surface heat flux is interactive (increases with wind speed), compared to a fixed surface heat flux simulation. The smaller cold pools are explained as a faster recovery of the gust front buoyancy due to the stronger surface heat flux there. Böing et al. (2012) showed that an imposed damping of moisture and temperature in the mixed layer reduces the cold pool size and cloud spacing. Similarly, Nissen and Haerter (2021) found that a smaller rain evaporation rate reduces the cloud spacing. Schlemmer and Hohenegger (2014) qualitatively proposed an amplification mechanism of cold pools to explain the convective deepening in the diurnal cycle: wider clouds have smaller entrainment and could produce wider cold pools, which trigger even wider clouds.

The above puzzles drive us to ponder the nature of precipitating convection. The prototype model of convection is Rayleigh-Bénard convection, which is the fluid convection between a pair of parallel plates, with the lower plate warm and the upper plate cold (Chandrasekhar 2013). This kind of convection is stationary, which means that a warm perturbation at one place grows steadily in positive feedback, without changing phase. The diffusion and viscosity damp the short-wave mode, and the perturbation pressure gradient force damps the long-wave mode. Thus, an optimal mode (most unstable mode) exists that characterizes the convective cell pattern. This has been applied to explain the spacing of shallow cumulus clouds which reflects the length scale of the boundary layer convective cell (Thuburn and Efstathiou 2020; Öktem and Romps 2021). For precipitating convection, however, the precipitation-driven downdraft kills the updraft. The mixed layer needs some time to recover before the next cycle begins (Daleu et al. 2020). This oscillatory feature differs from the stationary feature of Rayleigh-Bénard convection, as has been discussed by Feingold et al. (2010). Despite the difference, can we also explain the spacing of deep convection as an optimal mode?

Previous works have studied the hydrodynamic instability of moist convection without considering the trigger of new convection by cold pools (Kuo 1961; Emanuel 1986; Bretherton 1987; Hernandez-Duenas et al. 2015; Fu 2021). They start from the Navier-Stokes equation and treat the pressure gradient force in a self-consistent way, but these frameworks cannot accurately address strongly nonlinear phenomena like the updraft plume and cold pool. Instead, precipitating convection with cold pools has been studied with simpler nonlinear oscillator models at a phenomenological level. For example, Koren and Feingold (2011) considered precipitating convection as an accumulation-consumption cycle of cloud water content, and Feingold and Koren (2013) considered the nonlocal triggering effect from neighboring clouds as a delay function of the neighboring convective strength. The cloud spacing is prescribed, rather than solved. A desirable framework should physically parameterize the nonlinear processes but retain the analytical tractability and a holistic view. Some stratocumulus cloud models have such a flavor (Fielder 1984; Breidenthal and Baker 1985), but we are unaware of any precipitating convection model on this track.

In this paper, we consider the convective life-cycle to be controlled by a pair of thermodynamic and dynamical variables with a parameterized convective trigger process. The thermodynamic variable is the mixed layer equivalent potential temperature. The dynamical variable is piecewise. It denotes downdraft strength in the convective phase and denotes gust front speed in the recovery phase. They constitute a novel piecewise linear oscillator - a kind of nonlinear oscillator whose restoring force is a piecewise linear function of the phase (Shaw and Holmes 1983). As far as we know, this concept is new to atmospheric convection study. We use the piecewise oscillator as an "operator" that solves the cloud spacing as an optimal perturbation from the maximum cold pool size predicted by Romps and Jeevanjee (2016). If the recovery is complete, the gust front speed will reduce to zero upon transitioning to the convective phase, and the cold pool will reach its maximum size which we consider to obey the prediction of Romps and Jeevanjee (2016). In equilibrium deep convection, the recovery is incomplete. This is represented as a cutoff that behaves as a damping factor on the mixed layer equivalent potential temperature. At the same time, the gust front can collide and amplify convection. The theory predicts an optimal cloud spacing and recovery status that make the system most unstable. The optimal spacing is predicted to be limited by the cold pool entrainment length scale, which explains why the cloud spacing diagnosed from large-eddy simulations (LES) deviates more and more from the maximum cold pool size as rain evaporation rate increases.

As for the organization of this paper, section 2 introduces our novel piecewise linear oscillator model of convective life-cycle and how it leads to a theory of cloud spacing. Section 3 compares the theory with LES. Section 4 concludes the paper.

2. A piecewise linear oscillator model of convective life-cycle

a. Motivation

To contextualize the analytical treatment, the basic flow pattern of the numerical control run simulation is introduced first. It is a 96×96 km^2 LES over a 300 K sea surface in a doubly periodic domain. The details of the setup are introduced in section 3a. As an example, Fig. 1

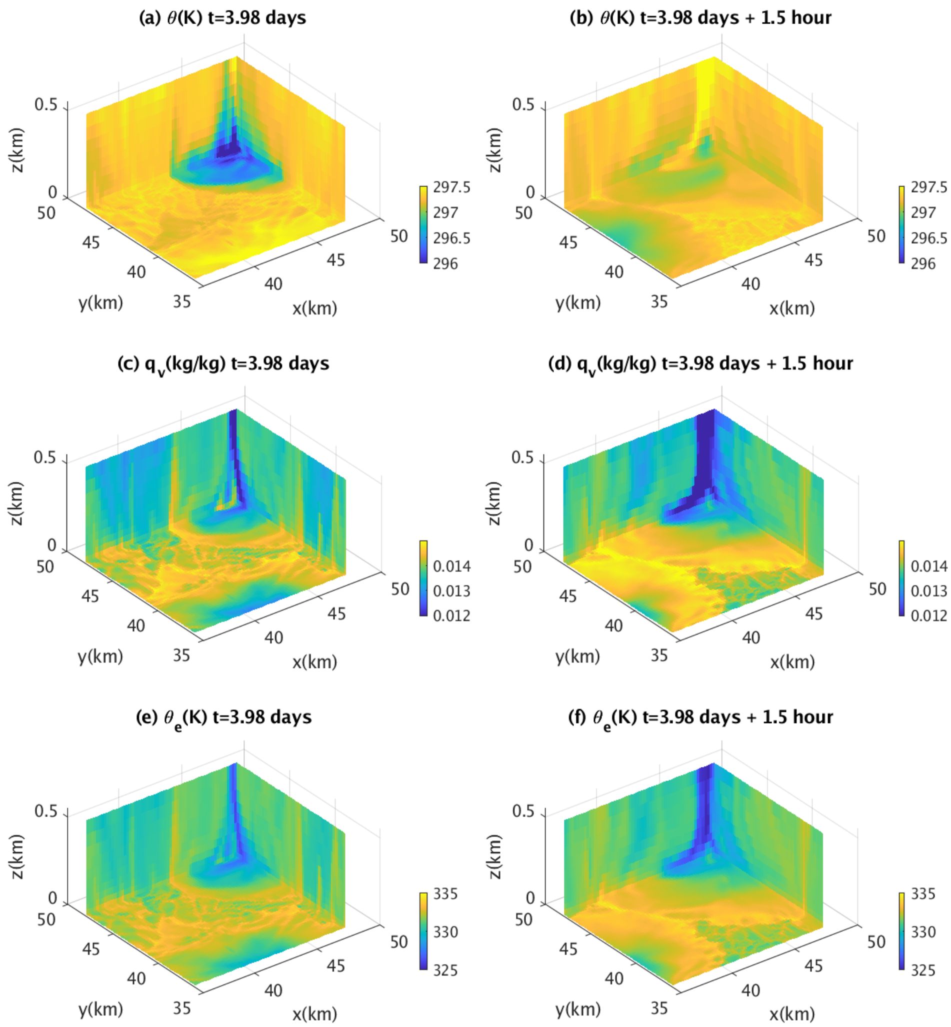

Fig. 1. The 3D structure of a cold pool in the SST= 300 K large-eddy simulation at day 3.98 and 1.5 hours later. The cold pool is chosen by selecting a near-surface low potential temperature region near day 4. The details of the LES setup are introduced in section 3a. (a) Potential temperature θ (unit: K) at day 4. (b) The θ 1.5 hours later. (c) Water vapor mixing ratio q_v (unit: g kg^{-1}) at day 3.98. (d) The q_v 1.5 hours later. (e) Equivalent potential temperature θ_e (unit: K) at day 3.98. (f) The θ_e 1.5 hours later. The θ_e is calculated with equation (4.5.11) of Emanuel (1994) which is relatively accurate.

shows the 3D structure of a cold pool. The gust front is a water vapor ring because the front forms in a rain shaft and further gains water vapor via surface flux (Langhans and Romps 2015). The equivalent potential temperature θ_e denotes the highest potential temperature a parcel could attain in an adiabatic ascending process. An approximate expression of θ_e is:

$$\theta_e \approx \theta \exp\left(\frac{L_v q_v}{c_p T}\right), \tag{1}$$

where θ is potential temperature, L_v is the vapor latent heat, c_p is the isobaric specific heat of dry air, and T is temperature (Marshall and Plumb 2016). Note that we use a more accurate formula of θ_e (Emanuel 1994) in the diagnosis of LES. In the mixed layer, the equivalent potential temperature (θ_e) field is dominated by the water vapor (q_v) distribution (Fig. 1).

The gust front θ_e, and a joint dynamical variable that alternatively represents the mixed layer top downdraft velocity w_d and gust front velocity u, are chosen as the two prognostic variables of our precipitating convection model. We do not consider free-tropospheric variables for two reasons.

- There is little free tropospheric buoyancy gradient and memory due to the fast gravity wave adjustment (Emanuel 1994).
- Convection indeed leaves a moisture anomaly in the free troposphere which can reduce the entrainment cooling of future convection. However, convection and its moisture remnant only takes a small fractional area. A small perturbation to the position of next convection can miss this moisture patch.

Thus, following Mapes (1993), we consider θ_e as a buoyancy variable is sufficient to qualitatively measure the potential convective strength. The downdraft brings down low θ_e air from the midlevel, which gradually recovers due to wind-induced surface heat fluxes and cold pool entrainment. The prognostic variables serve as a thermodynamic-dynamical pair that oscillate around their time-averaged basic state. The thermodynamic basic state value $\overline{\theta_e}$ is assumed to equal the mixed layer equivalent potential temperature outside of the cold pool. We let $\theta_e' = \theta_e - \overline{\theta_e}$ be the perturbation part of the gust front equivalent potential temperature. The θ_e' should not only represent the narrow frontal region, but also a finite-thickness ring of the cold air behind the gust front. This is because the air there will also be involved in the updraft upon cold pool collision (Fuglestvedt and Haerter 2020).

The Hövmoller diagram (Fig. 2) confirms that the triggering of most of the events are associated with the passage of at least one active gust front. Convection is a highly intermittent event that only takes a small fraction of the space and time. Each convective event has an updraft burst followed by a downdraft.

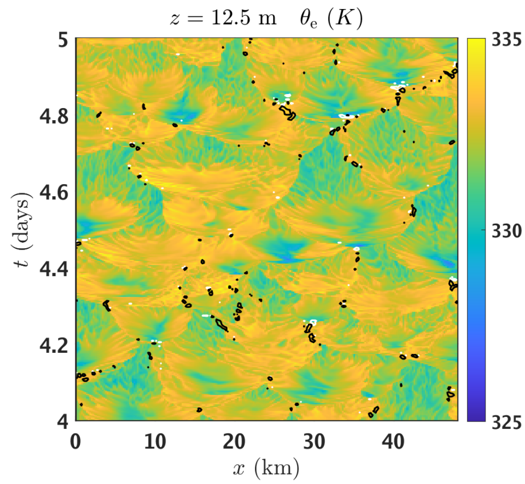

FIG. 2. The Hövmoller diagram of the $z = 12.5$ m equivalent potential temperature (filled map) and $z = 825$ m vertical velocity which is above the mixed layer top (white line for -0.7 m s^{-1} and black line for 1 m s^{-1} contour). The data uses the $y = 48$ km cross-section of the control run. Only the data between $x = 0$ km and $x = 48$ km from day 4 to day 5 are displayed. This figure shows that an updraft event is followed by a downdraft, and the convective phase is much shorter than the recovery phase.

b. A piecewise linear oscillator

The oscillation is split into two parts. The first part is the convective phase which takes a short time Δt_+, and the second part is the recovery phase which takes a much longer time Δt_-. The period of the oscillation is their sum: $\Delta t = \Delta t_+ + \Delta t_-$. Without the gust front lifting effect, the cold pool θ_e will recover to the environmental value before the new convection occurs. The maximum cold pool radius l_m, which is the gust front traveling length needed for it to recover to zero potential temperature difference with the environment, was theoretically studied by Romps and Jeevanjee (2016), and hence referred to as RJ16 model. Because the θ_e accumulation of the cold pool relies on the gust front movement, the maximum cold pool size also sets the maximum θ_e that can be gained in a cold pool event. With the gust front lifting which is an additional forcing, the θ_e need not recover to the maximum value. What sets the cold pool size in this case?

We hypothesize that there is an optimal length l_c that is smaller than the maximum cold pool size l_m. If the length is too short, the low θ_e from a recent downdraft cannot support deep convection at all. We conceptualize it as a piecewise linear oscillator with a cutoff (denoted as "PLOC"). The case where gust front lifting is absent is described as a piecewise linear oscillator without cutoff (denoted as "PLO"), where the gust front velocity decreases to zero at the beginning of a new convective life-cycle. When there is gust front triggering, boundary layer θ_e is released by convection before it can naturally reach the maximum value, and this early triggering is denoted as a "cutoff". We will show that the incomplete recovery of boundary layer θ_e is a damping effect. To make the oscillator in equilibrium, the incomplete recovery, as well as the damping due to cold pool entrainment that will be discussed, should be compensated by the destabilizing effect due to the lifting effect of a gust front. The idea is to use the PLOC model to solve the optimal cloud spacing l_c as a perturbation from the well-established l_m which involves detailed fluid dynamics of a cold pool (Romps and Jeevanjee 2016):

$$\text{RJ16 cold pool model :} \quad l_m = \left(\frac{9V_0}{2\pi C_E} \frac{\theta_{ml} - \theta_{ini}}{\theta_{surf} - \theta_{ini}} \right)^{1/3}, \tag{2}$$

where V_0 is the initial volume of a cylindrical cold pool. It equals $V_0 = 2\pi l_0 H_0$, where l_0 is the initial radius of the cold pool and H_0 is the initial height of the cold pool. The θ_{ini} is the initial potential temperature of the gust front, θ_{ml} is the mixed layer environmental potential temperature, and θ_{surf} is the sea surface temperature. The length scale l_m does not depend on the cold pool fractional entrainment rate ε, because entrainment dilutes the cold air but does not change the total amount of heat needed to eliminate the cold anomaly (Romps and Jeevanjee 2016).

In the convective phase ($0 < t < \Delta t_+$), θ_e starts from the maximum value. The convective instability induces convection and therefore downdraft velocity w_d which reduces θ_e to the minimum value. The downdraft velocity w_d first increases from zero and then decreases to zero. Note that w_d is a non-negative variable. The θ_e' equation is derived by linearizing the conservation law of θ_e:

$$\text{convective phase :} \quad \frac{d\theta_e'}{dt} = -\frac{\alpha_+ \Delta\theta_e}{H_c} w_d. \tag{3}$$

Here H_c denotes the cold pool height. Because gravity current in a vertically confined channel like the mixed layer tends to occupy half the depth (Emanuel 1994), we prescribe it as a constant value $H_c = H_m/2$, where $H_m \approx 600$ m is the mixed layer depth. The downdraft drying term is multiplied by a parameter α_+ which is the updraft fractional area, because we assume the dry air from the downdraft spreads immediately in the mixed layer upon reaching the surface. This is a lower bound of the influence of a downdraft at the convective site. A more realistic estimation involves the spreading speed of the cold pool, which will be considered in the future. Assuming that downdraft strength is proportional to updraft strength and there is no time delay between them, we use w_d to express the vertical momentum equation of the updraft branch as:

$$\text{convective phase :} \quad \frac{dw_d}{dt} = \gamma_+ \theta'_e + \frac{w_d}{\tau_{w+}}. \tag{4}$$

Here γ_+ is a parameter that measures the ability of high θ'_e mixed layer air to generate a downdraft, analogous to the role of the thermal expansion coefficient in a fluid parcel's buoyancy. Equation (A4) in the appendix provides an estimate of γ_+. The τ_{w+} is the dynamical lifting time scale that is proportional to the gust front velocity at the trigger point (u_*), a parameter to be discussed in more detail in section 2d. The w_d in the w_d/τ_{w+} term is the downdraft strength of the neighboring clouds $\Delta t_+ + \Delta t_-$ time ago. For a homogeneous convective state, a transformation in space and time shows that this strength is identical to the current strength of the cloud we study, as is illustrated in Fig. 3. Equations (3) and (4) yield an expression of Δt_+:

$$\Delta t_+ = \pi \left(\frac{\gamma_+ \alpha_+ \Delta\theta_e}{H_c} \right)^{-1/2}. \tag{5}$$

Two important factors have been omitted: the drag on the updraft which serves as a damping factor, and the delay of the transition from downdraft to updraft. The latter will be shown to represent convective instability. Recently, there is growing evidence that thermals are in balance between buoyancy and drag (Romps and Charn 2015; Romps and Öktem 2015). In the appendix, we separately treat updrafts and downdrafts and use this argument to show that the damping effect of drag and the amplifying effect of the downdraft delay may cancel each other in the oscillator.

The other half of the life-cycle is the recovery phase ($-\Delta t_- \leq t \leq 0$). The dynamical variable is switched from w_d to gust front speed u, and the thermodynamic variable remains θ'_e. The gust front

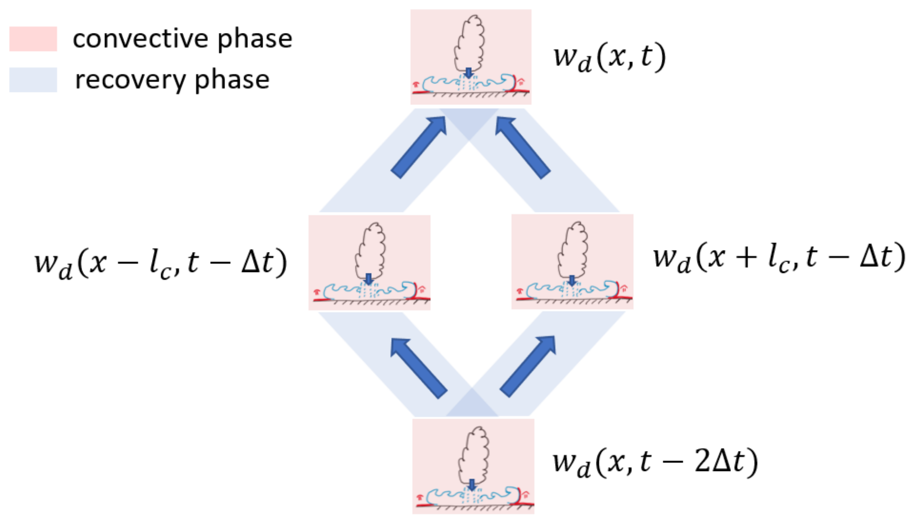

FIG. 3. A schematic diagram of the oscillator model. The period of the oscillator consists of a convective and a recovery phase, which is denoted as the red and blue shadow. Note that the recovery phase depicts the gust front, which is marked with the large blue arrow. The downdraft strength of the cloud of interest (at position x and time t) depends on the downdraft strength of two neighboring clouds Δt time ago. The cloud spacing is denoted as l_c. It takes $2\Delta t$ time for convection to re-appear at the same location. The homogeneous and quasi-equilibrium condition indicate that $w_d(x,t) = [w_d(x-l_c,t-\Delta t)+w_d(x+l_c,t-\Delta t)]/2 = w_d(x,t-2\Delta t)$.

speed u first accelerates due to the conversion from potential energy to kinetic energy, and then decelerates due to the recovery process that reduces the potential temperature difference between the cold pool and the environment. The system is considered to transition to the recovery phase when u reduces to a trigger velocity u_*, rather than zero. The θ_e' and u equations in this phase are:

$$\text{recovery phase}: \quad \frac{d\theta_e'}{dt} = -\frac{\theta_e'}{\tau_{e-}} + \frac{C_E}{H_c}\left(\theta_{es} - \overline{\theta_e}\right)u, \tag{6}$$

$$\text{recovery phase}: \quad \frac{du}{dt} = -\gamma_- \theta_e', \tag{7}$$

where γ_- is a parameter that relates the gust front θ_e' to its horizontal acceleration, conceptually analogous to γ_+ in the convective phase. In the numerical integration of PLOC, this transition point is identified when $u = u_*$ and $\theta_e' > 0$. Then, the convective phase starts with $w_d = 0$. In contrast, θ_e' is continuous throughout the life-cycle. The parameter C_E is the surface heat exchange coefficient, θ_{es} is the equivalent potential temperature at the saturated sea surface, and ε is the cold pool fractional entrainment rate which has been mentioned. They are viewed as constants. Note that we have assumed the mixed layer equivalent potential temperature outside of the cold pool to equal $\overline{\theta_e}$. The u term in (6) denotes the wind-dependent part of surface heat flux. The τ_{e-} in (8) is the mixed layer relaxation time scale, which includes the cold pool entrainment and the θ_e'-dependent part of surface heat flux:

$$\tau_{e-} \equiv \left(\varepsilon u_c + \frac{C_E u_c}{H_c}\right)^{-1} \approx (\varepsilon u_c)^{-1}, \tag{8}$$

where u_c is the gust front characteristic speed. Here we follow Romps and Jeevanjee (2016) to neglect the surface flux component. This is valid because $\varepsilon \ll C_E/H_c$ for $\varepsilon \approx 2\times 10^{-4}$ m^{-1}, $C_E \approx 0.004$ (as a variable in our LES) and $H_c \approx 300$ m.

The gust front characteristic speed u_c is considered to take the mean value of u in the recovery phase:

$$u_c = \frac{1}{\Delta t_-}\int_{-\Delta t_-}^{0} u dt = \frac{1}{\Delta t_-}\int_{-\Delta t_-}^{0} \sin\left(\pi \frac{t}{\Delta t_-}\right) dt = \frac{u_m}{\pi}, \tag{9}$$

where u_m is the maximum gust front velocity. We have used a harmonic-shape u in deriving (9), and the integration covers a half-period. Note that u represents the potential temperature deficit of the cold pool, due to the inertial-buoyancy balance at the gust front (Ungarish 2009):

$$u^2 = \mathrm{Fr}^2 g \frac{\theta - \theta_{ml}}{\theta_{ml}} H_c, \tag{10}$$

where $g = 9.8$ m s^{-2} is gravitational acceleration and Fr is Froude number which is around unity (Ross et al. 2004). When the gust front potential temperature fully recovers to the environmental value, u is strictly zero corresponding to (10). The u could also take a small value if the momentum tendency is considered (Romps and Jeevanjee 2016), which is neglected here.

Cold pool entrainment is a damping effect on θ_e'. At the early stage of the cold pool, low θ_e air flows behind a thin rain-induced high θ_e arc (Fig. 1e). Because θ_e' represents the perturbation equivalent potential temperature not only at the front but also a finite-thickness ring behind it, it is not obvious whether entrainment increases or decreases it. At the mature stage, the surface heat flux generates a broad band of high θ_e air near the gust front, so entrainment reduces θ_e' (Fig. 1f). In contrast, the potential temperature of a gust front always experiences an increase by entrainment because it is always lower than the environmental value (Fig. 1a and b), as is implicitly indicated by the factor γ_-. This is explained in more detail below.

Equation (7) considers the gust front's horizontal motion to be analogous to the parcel vertical motion driven by buoyancy, where u is accelerated to u_m by the recovery of θ_e' and then decelerates. Although there are indeed fundamental links between the buoyancy-driven horizontal and vertical plume (Turner 1986), this specific comparison is physically inaccurate. Unlike the tendency-buoyancy balance in (7), buoyancy-driven horizontal flow is in inertial-buoyancy balance (10) instead, which leads to a gust front. The u attains the maximum value right after the cold pool forms due to the lowest $\theta-\theta_{ml}$ at that moment (Romps and Jeevanjee 2016). Then, the magnitude of u and $\theta-\theta_{ml}$ slowly reduce by surface heating and entrainment. The use of (7) makes the model a mathematically elegant oscillator by sacrificing some physical accuracy. Because (7) does not quantitatively depict the dynamics, we consider the time duration of the recovery phase to be the cold pool propagation time across the maximum cold pool size (l_m/u_c) and retrieve γ_- from it:

$$\Delta t_- = \pi\left[\gamma_-\frac{C_E}{H_c}\left(\theta_{es}-\overline{\theta_e}\right)\right]^{-1/2} \sim \frac{l_m}{u_c}. \tag{11}$$

The above analysis shows that the recovery phase of the oscillator model is only a coarse representation of the cold pool dynamics, which is far less complete than the RJ16 model. Our motivation is to use the oscillator as a tool to map the maximum cold pool size predicted by the RJ16 model to the equilibrium deep convection. When $u_* = 0$ ($\tau_{w+}\to\infty$) and $\tau_{e-}\to\infty$, the PLOC reduces to a neutral PLO, and the cloud distance is considered to take the maximum value l_m. In section 3c, we nondimensionalize the PLOC and analyze the numerical integration result.

c. The nondimensional formulation and comparison with simulation

To reveal the mathematical skeleton of the piecewise linear oscillator (with cutoff), we need to nondimensionalize (3), (4), (6), and (7). We use Θ, $\mathcal{W}$, and Δt to nondimensionalize θ_e', w_d, and time t:

$$\theta_e' = \Theta\widetilde{\theta_e'},\ w_d = \mathcal{W}\widetilde{w_d},\ t = \Delta t\widetilde{t}. \tag{12}$$

where $\widetilde{\theta_e'}$, $\widetilde{w_d}$ and $\widetilde{t}$ are the nondimensionalized quantities. The key procedure that combines the two dynamical variables w_d and u into one is to extend the domain of definition of w_d to the recovery phase by assigning it as a rescaled u, using (3) and (6):

$$\text{recovery phase}: \; w_d = -u \frac{\frac{C_E}{H_c}\left(\theta_{es} - \overline{\theta_e}\right)}{\alpha_+ \Delta\theta_e / H_c}, \quad w_d < 0. \tag{13}$$

Substituting (12) and (13) into (3), (4), (6), and (7), we get:

$$\frac{d\widetilde{\theta'_e}}{d\widetilde{t}} = -\widetilde{\alpha}\widetilde{w_d} + \begin{cases} 0, & \widetilde{w_d} \geq 0, \\ -\frac{\widetilde{\theta'_e}}{\widetilde{\tau_{e-}}}, & \widetilde{w_d} < 0, \end{cases} \tag{14}$$

$$\frac{d\widetilde{w_d}}{d\widetilde{t}} = \begin{cases} \widetilde{\gamma_+}\widetilde{\theta'_e} + \frac{\widetilde{w_d}}{\widetilde{\tau_{w+}}}, & \widetilde{w_d} \geq 0, \\ \widetilde{\gamma_-}\widetilde{\theta'_e}, & \widetilde{w_d} < 0, \end{cases} \tag{15}$$

The transition from the recovery phase to the convective phase occurs when $\widetilde{w_d}$ reaches $\widetilde{w_d^*}$ from below. The expression of nondimensional parameters $\widetilde{\alpha}$, $\widetilde{\gamma_+}$, $\widetilde{\gamma_-}$, $\widetilde{w_d^*}$, $\widetilde{\tau_{w+}}$, and $\widetilde{\tau_{e-}}$ are:

$$\widetilde{\alpha} = \frac{\alpha_+ \Delta\theta_e}{H_c} \frac{\mathcal{W}}{\Theta} \Delta t, \tag{16}$$

$$\widetilde{\gamma_+} = \frac{\Theta}{\mathcal{W}} \Delta t \gamma_+, \tag{17}$$

$$\widetilde{\gamma_-} = \frac{\frac{C_E}{H_c}\left(\theta_{es} - \overline{\theta_e}\right)}{\alpha_+ \Delta\theta_e / H_c} \frac{\Theta}{\mathcal{W}} \Delta t \gamma_-, \tag{18}$$

$$\widetilde{w_d^*} = -\frac{\frac{C_E}{H_c}\left(\theta_{es} - \overline{\theta_e}\right)}{\alpha_+ \Delta\theta_e / H_c} \frac{u_*}{\mathcal{W}}, \tag{19}$$

$$\widetilde{\tau_{w+}} = \frac{\tau_{w+}}{\Delta t}, \tag{20}$$

$$\widetilde{\tau_{e-}} = \frac{\tau_{e-}}{\Delta t}. \tag{21}$$

To guarantee that the nondimensional oscillation period is unity, there is a constraint between α, $\widetilde{\gamma_-}$, and $\widetilde{\gamma_-}$:

$$\underbrace{\frac{\pi}{(\widetilde{\gamma_+}\widetilde{\alpha})^{1/2}}}_{\Delta t_+/\Delta t} + \underbrace{\frac{\pi}{(\widetilde{\gamma_-}\widetilde{\alpha})^{1/2}}}_{\Delta t_-/\Delta t} = 1. \tag{22}$$

We perform a numerical integration of (14) and (15), with the initial condition set at $\widetilde{t} = -\Delta t_-/\Delta t$, which is the start of the recovery phase:

$$\widetilde{\theta'_e}|_{\widetilde{t}=-\Delta t_-/\Delta t} = -\widetilde{\gamma_-}^{-1/2}, \quad \widetilde{w_d}|_{\widetilde{t}=-\Delta t_-/\Delta t} = 0. \tag{23}$$

The parameters are $\widetilde{\alpha} = 1$, $\widetilde{\gamma_+} = 25\pi^2/\widetilde{\alpha}$, and $\widetilde{\gamma_-} = (25/16)(\pi^2/\widetilde{\alpha})$. Note that $\widetilde{\alpha} = 1$ and (23) are set by properly choosing $\mathcal{W}$ and Θ, which are two free parameters. When the cutoff is not considered ($\widetilde{w_d^*} = 0$), the parameter setting and initial condition yield a minimum $\widetilde{w_d}$ value of $\min\{\widetilde{w_d}\} = -1$, and a maximum value of $\max\{\widetilde{w_d}\} = \Delta t_-/\Delta t_+ = 4$. The $\min\{\widetilde{w_d}\} = -1$ property can be used to simplify the expression of (19). Using the definition of maximum gust front speed: $\max\{u\} = u_m$ and (13), we get:

$$\widetilde{w_d^*} = -\frac{u_*}{u_m}. \tag{24}$$

We perform some demonstration of the oscillator in Fig. 4. To make the demonstration clean, we temporarily omit the gust front triggering effect and the cold pool entrainment damping by setting $\widetilde{\tau_{w_+}} \to \infty$ and $\widetilde{\tau_{e_-}} \to \infty$. The PLO simulation with $\widetilde{w_d^*} = 0$ is shown in Fig. 4a, which is essentially a stretched harmonic oscillator. The time duration difference between the (slow) heat accumulation phase and (fast) consumption phase has been attributed to a microphysics-related quadratic term in the oscillator model of shallow precipitating convection (Koren and Feingold 2011; Koren et al. 2017). We argue that a piecewise oscillator, which considers the two phases to be of different physical processes (convection and gust front), is physically more relevant to the time duration difference in our case of deep convection.

For the PLOC simulation where the recovery is incomplete, we set $\widetilde{w_d^*} = -0.2$. Figure 4b shows that the oscillator is damped. This is because when $\widetilde{w_d}$ reaches $\widetilde{w_d^*}$ from below in the recovery phase, $\widetilde{\theta'_e}$ attains its maximum value which is smaller than the magnitude of its minimum value at the beginning of the recovery phase. For the next convective phase without a cutoff, the next minimum value will equal the maximum value that has just been attained. This explains the reduction of amplitude in subsequent cycles. Can we quantify this damping? Could it be balanced by the destabilizing effect of the gust front lifting ($\widetilde{\tau_{w_+}}$)?

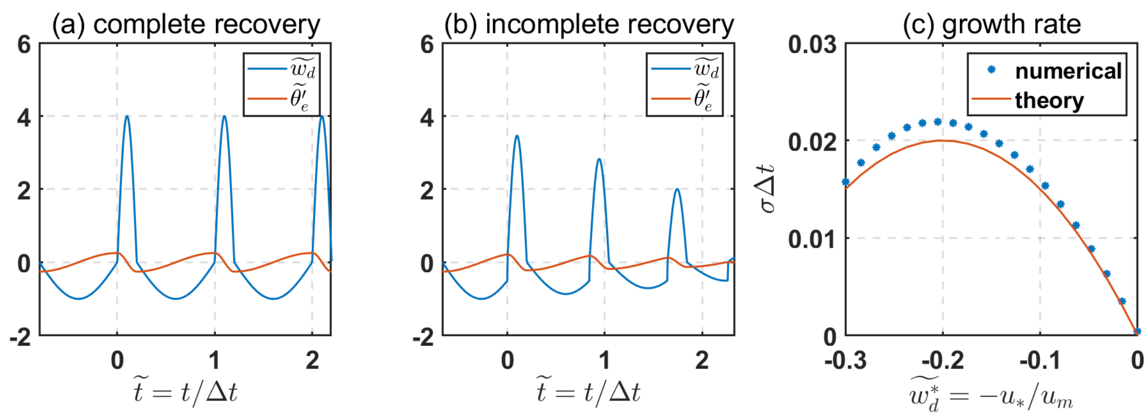

FIG. 4. (a) The numerical integration of the piecewise linear oscillator (PLO) in nondimensional form, using $\widetilde{\alpha} = 1$, $\widetilde{\gamma_+} = 25\pi^2/\widetilde{\alpha}$, $\widetilde{\gamma_-} = (25/16)(\pi^2/\widetilde{\alpha})$, $\widetilde{\tau_{w+}} \to \infty$, $\widetilde{\tau_{e-}} \to \infty$, and $\widetilde{w_d^*} = 0$. The gust front is completely dissipated by the start of the convective phase. The blue line denotes $\widetilde{w_d}$, and the red line denotes $\widetilde{\theta'_e}$. (b) The same as (a), but for a piecewise linear oscillator with cutoff (PLOC), with $\widetilde{w_d^*} = -0.5$ which accounts for the incomplete recovery. (c) The blue "*" denotes the growth rate of a series of numerical integrations with different $\widetilde{w_d^*}$. To isolate the triggering and incomplete recovery effect, we set $\widetilde{\tau_{e-}} \to \infty$. The growth rate is diagnosed with $\sigma = \ln(\widetilde{w_2}/\widetilde{w_1})/(\widetilde{t_2} - \widetilde{t_1})$, where $\widetilde{w_1}$ and $\widetilde{w_2}$ are the first and second maximum value of $\widetilde{w_d}$ in the time series that occurs at $\widetilde{t} = \widetilde{t_1}$ and $\widetilde{t} = \widetilde{t_2}$. The red line denotes the theoretical prediction, which is introduced in section 2d.

d. The optimal mode

Next, we consider the role of nonzero u_* in setting the optimal cloud spacing. We let t' and l' be the perturbation time and perturbation distance that the system exhibits before the full recovery. Thus, we consider $\Delta t_- - t'$ to be the time duration of the recovery phase and define $l_c \equiv l_m - l'$ as the cloud spacing. The expressions of u_* and l' are a function of t', using a small perturbation assumption ($t' \ll \Delta t_-$):

$$u_* = u_m \sin\left(\pi \frac{t'}{\Delta t_-}\right) \approx u_m \pi \frac{t'}{\Delta t_-}, \tag{25}$$

$$l' = \int_0^{t'} u dt = u_m \int_0^{t'} \sin\left(\pi \frac{t}{\Delta t_-}\right) dt \approx u_m \frac{\pi}{2} \frac{t'^2}{\Delta t_-}. \tag{26}$$

The finite u_* introduces a finite τ_{w+} which amplifies the system, while the cutoff on the recovery of θ'_e damps the system. This small perturbation treatment is illustrated in Fig. 5.

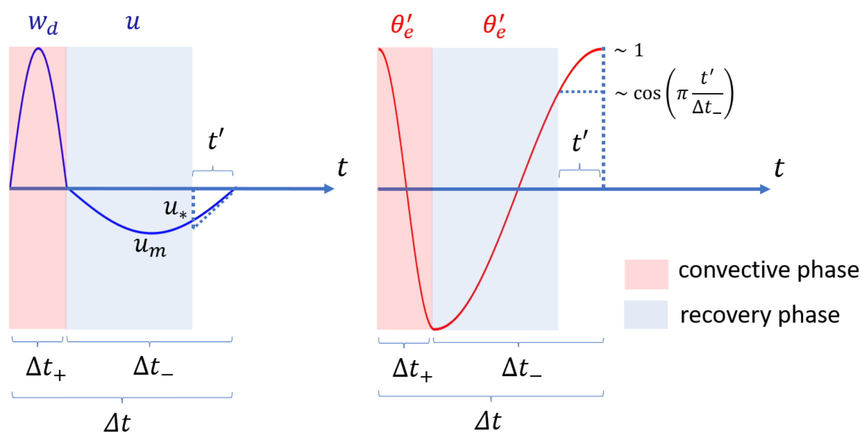

FIG. 5. A schematic diagram of the small perturbation treatment in deriving the optimal mode. The damping due to cold pool entrainment and the amplification due to triggering are not included in the sketch. The red and blue shadow denote the convective and recovery phase respectively. The left panel shows the dynamical variables w_d and u, and the right panel shows the thermodynamic variable θ'_e. The $t' \ll \Delta t_- \approx \Delta t$ assumption will be repetitively used in the theoretical derivation.

The growth rate of the system (3) (4) (6) (7), which is denoted as σ, is determined by the destabilizing and stabilizing factors in the convective phase (Δt_+) and recovery phase ($\Delta t_- - t' \approx \Delta t_-$) distributed over the whole life-cycle ($\Delta t = \Delta t_+ + \Delta t_-$). It has been proposed as a potential general rule that quasi-equilibrium fluid convection is dominated by its most unstable (optimal mode), which must have a zero growth rate (e.g. Thuburn and Efstathiou 2020):

$$\sigma = \max\{\sigma\} = 0. \tag{27}$$

This requires us to quantify all the other stabilizing and destabilizing effects. We consider the dissipation on the updraft to balance with the convective instability of the plume offered by the precipitation delay, as is discussed in the appendix. This leads to a balance between gust front lifting, incomplete recovery, and cold pool entrainment damping:

$$\sigma = \frac{1}{\tau_w} - \frac{1}{\tau_{cut}} - \frac{1}{\tau_e}, \tag{28}$$

where τ_w, τ_{cut}, and τ_e are the bulk amplification timescale of gust front triggering, the bulk damping timescale of incomplete recovery due to cutoff, and the bulk damping timescale of cold pool entrainment.

The bulk trigger amplification timescale τ_w is related to τ_{w+} with a rescaling:

$$\tau_w = \tau_{w+} \frac{2\Delta t}{\Delta t_+}. \tag{29}$$

Here a factor of 2 is introduced because the lifting effect is imposed only on w_d and not on θ'_e, and therefore the effect on the system is halved. A dilution factor of $\Delta t / \Delta t_+$ is introduced because the triggering only works in the convective phase rather than the whole life-cycle.

Similarly, the bulk damping effect of cold pool entrainment, which only works on θ'_e in the recovery phase, is denoted as τ_e. It is related to τ_{e-} with a rescaling:

$$\tau_e = \tau_{e-} \frac{2\Delta t}{\Delta t_-}. \tag{30}$$

The cold pool entrainment time scale $\tau_{e-} \approx (\varepsilon u_c)^{-1}$ is not a function of t', so it is the dominant stabilizing effect of the oscillator. It results from the heat exchange between the cold pool and the mixed layer environment which serves as a thermal reservoir.

We focus on the competition between the bulk triggering time scale τ_w and the damping due to incomplete recovery τ_{cut}, because we will show that both of them would be infinite if $t' = 0$.

Instead of directly studying τ_{w+}, we propose an expression of τ_w by considering dynamical lifting as a feedback loop. The fractional growth due to dynamical lifting in one life-cycle period is expressed as $e^{\Delta t / \tau_w} - 1$, which depends on how the lifting-contributed part of the downdraft at the current cycle (denoted as Δw_d^n) depends on the downdraft at the previous cycle (denoted as w_d^{n-1}):

$$e^{\frac{\Delta t}{\tau_w}} - 1 = \frac{\partial \Delta w_d^n}{\partial w_d^{n-1}} = \frac{\partial \Delta w_d^n}{\partial u_*^{n-1}} \frac{\partial u_*^{n-1}}{\partial u_m^{n-1}} \frac{\partial u_m^{n-1}}{\partial w_d^{n-1}}. \tag{31}$$

Here u_*^{n-1} denotes the trigger velocity of the gust front of the previous cycle, and u_m^{n-1} denotes its maximum gust front velocity. Next, we simplify the derivative chain. The horizontal velocity and vertical velocity are linked with fluid continuity. Letting l_0 be the cloud base radius, we define the mixed layer top updraft velocity of the current cycle as w_{uT}^n which obeys:

$$\text{continuity}: \quad w_{uT}^n \equiv \frac{2\pi l_0 H_c}{\pi l_0^2} u_*^{n-1} = \frac{2H_c}{l_0} u_*^{n-1}, \tag{32}$$

where $2\pi l_0 H_c$ is the lateral area of the updraft cylinder in the mixed layer, and πl_0^2 is the cloud bottom area. Not all the gust front air turns into updraft, but we consider the mixed layer top mass flux to be at least proportional to the gust front mass flux entering the convective site. This is because the gust front carries mixed layer thermals which fuel the updraft. Analogously, for the downdraft we have:

$$\text{continuity}: \quad \frac{\partial u_m^{n-1}}{\partial w_d^{n-1}} = \frac{l_0}{2H_c}. \tag{33}$$

Considering a relatively weak lifting effect ($\Delta t \ll \tau_w$) and $\partial u_*^{n-1}/\partial u_m^{n-1} \approx u_*/u_m$, which is a key linear assumption, and substituting (32) and (33) into (31), we get:

$$\frac{1}{\tau_w} \approx \frac{u_*}{u_m \Delta t} \frac{\partial \Delta w_d^n}{\partial u_*^{n-1}} \frac{\partial u_m^{n-1}}{\partial w_d^{n-1}} \approx \frac{u_*}{l_m} \underbrace{\frac{1}{\pi} \frac{\partial \Delta w_d^n}{\partial w_{uT}^n}}_{\mu_*}, \tag{34}$$

where we have used (9) and ($\Delta t_- \approx \Delta t$) to get $l_m = u_c \Delta t_- = u_m \Delta t_- / \pi \approx u_m \Delta t / \pi$. We call the nondimensional parameter μ_* the downdraft-trigger efficiency. The quantity $\partial \Delta w_d^n / \partial w_{uT}^n$ denotes the downdraft production ability due to lifting, which still lacks a theoretical model. We surmise that μ_* depends on the convective trigger process (Grandpeix and Lafore 2010; Rio et al. 2013) and precipitating efficiency (Emanuel et al. 2014; Langhans et al. 2015; Lutsko and Cronin 2018; Fu and Lin 2019).

The cutoff time scale τ_{cut} is measured by the fractional reduction of θ_e' amplitude due to the incomplete recovery (Fig. 5):

$$e^{-\frac{\Delta t}{\tau_{cut}}} = \frac{\left|\theta_e'|_{t=0}\right|}{\left|\theta_e'|_{t=-\Delta t_-}\right|} = \frac{\left|\cos\left[\pi(-\frac{t'}{\Delta t_-})\right]\right|}{|-1|} = \cos\left(\pi \frac{t'}{\Delta t_-}\right). \tag{35}$$

Assuming $t' \ll \Delta t_-$, we linearize (35) with respect to t':

$$\frac{1}{\tau_{cut}} \approx \frac{\pi^2}{2}\frac{1}{\Delta t}\left(\frac{t'}{\Delta t_-}\right)^2. \tag{36}$$

Why is the first order term of t' absent in (36)? This is because (25) shows that u_* is small for a small t', and the gust front is therefore inefficient in generating surface heat flux by the time of collision. The total surface heating missed due to the incomplete recovery scales as: $u_* t' \sim t'^2$. The damping due to incomplete recovery is analogous to the molecular diffusion in Rayleigh-Bénard convection, which damps the short-wave mode.

Substituting (34), (30), and (36) into (28), and using (25) and (26) to simplify the expression, we get:

$$\sigma = \frac{1}{\Delta t}\left[-\frac{\pi^2}{2}\underbrace{\left(\frac{t'}{\Delta t_-} - \mu_* \frac{\Delta t}{\Delta t_-}\right)^2}_{=0} + \underbrace{\frac{\mu_*^2 \pi^2}{2}\left(\frac{\Delta t}{\Delta t_-}\right)^2 - \frac{\Delta t_-}{2\tau_{e-}}}_{=0}\right]. \tag{37}$$

Equation (37) shows that σ takes a maximum value when $t' = \mu_* \Delta t$, which yields $l' = (\mu_*^2 \pi^2/2)(\Delta t/\Delta t_-)^2 l_m$ according to (26). This is the optimal mode, which has:

$$\text{optimal}: \quad l_c = l_m\left[1 - \frac{\mu_*^2 \pi^2}{2}\left(\frac{\Delta t}{\Delta t_-}\right)^2\right], \tag{38}$$

$$\text{optimal}: \quad u_* = u_m\left(\mu_* \pi \frac{\Delta t}{\Delta t_-}\right), \tag{39}$$

$$\text{optimal}: \quad \tau_w = \Delta t\left(\frac{1}{\mu_* \pi}\frac{\Delta t_-}{\Delta t}\right)^2, \tag{40}$$

where we have used (25) and (34) to derive (39) and (40).

The theory predicts that the cloud spacing l_c is smaller than the maximum cold pool size l_m by a factor that is proportional to the square of the downdraft-trigger efficiency μ_*. A larger μ_* leads to a shorter cloud spacing and a larger cold pool collision velocity.

The analytical theory is benchmarked against numerical integration of the nondimensional system (14) and (15), with (23) as the initial condition. We still use $\widetilde{\alpha} = 1$, $\widetilde{\gamma_+} = 25\pi^2/\widetilde{\alpha}$, $\widetilde{\gamma_-} = (25/16)(\pi^2/\widetilde{\alpha})$, neglect the damping due to cold pool entrainment ($\widetilde{\tau_{e-}} \to \infty$), but include the lifting effect ($\widetilde{\tau_{w_+}}$). The expression of $\widetilde{\tau_{w_+}}$ is obtained by substituting (29) and (34) into (20):

$$\widetilde{\tau_{w+}} = \frac{\tau_w}{\Delta t}\frac{\Delta t_+}{2\Delta t} = \frac{l_m}{\mu_* u_* \Delta t}\frac{\Delta t_+}{2\Delta t} = -\frac{1}{\mu_* \pi}\frac{1}{\widetilde{w_d^*}}\frac{\Delta t_-}{\Delta t}\frac{\Delta t_+}{2\Delta t}, \tag{41}$$

where we have additionally used (24): $\widetilde{w_d^*} = -u_*/u_m$ and (9): $u_m = \pi u_c = \pi l_m/\Delta t_-$. Note that (41) is not constrained to be the optimal mode. We set $\mu_* = 0.2(\Delta t_-/\Delta t)(1/\pi)$, which corresponds to an optimal mode of $\widetilde{w_d^*} = -0.2$ according to (39). The system growth rates of a series of numerical integrations with different $\widetilde{w_d^*}$ are shown in Fig. 4c. The theoretical growth rate in nondimensional form (with $\tau_{e-} \to \infty$) is calculated with (37): $\sigma\Delta t = \Delta t/\tau_w - \Delta t/\tau_{cut} = -\widetilde{w_d^*}(\mu_*\pi)(\Delta t/\Delta t_-) - \widetilde{w_d^*}^2/2$. The theory agrees well with the numerical integration, despite an underestimation of the growth rate which is likely due to the assumption of $t' \ll \Delta t_- \approx \Delta t$ in the theoretical derivation.

This simple model views equilibrium deep convection as a primary piecewise oscillation plus a pair of destabilizing and stabilizing factors that balance each other. In view of energetics, a part of the convective (downdraft) kinetic energy is reused by the gust front to ignite the next convection. This indicates that precipitating convection has both free and forced properties.

It remains unclear what determines μ_* and whether it is a function of l_c. A related work is the convective parameterization scheme based on the available lifting power (ALP) closure (Grandpeix and Lafore 2010; Rio et al. 2013) where the gust front and the mixed layer thermals together determine the convective mass flux. However, this scheme does not consider the triggering due to cold pool collision which is prevalent in tropical maritime deep convection (Torri and Kuang 2019), as well as the recent finding that cold pools can serve as a conveyor belt to aggregate the mixed layer thermals (Fuglestvedt and Haerter 2020). Thus, we do not test or use the ALP scheme to estimate μ_* in this paper. Is there a way to circumvent the detailed trigger process?

We hypothesize that the μ_* can also be constrained by the zero growth rate argument which has not been used yet. Prescribing $\sigma = \max\{\sigma\} = 0$ in (37), we get:

$$\frac{1}{\tau_w} = \frac{2}{\tau_{cut}} = \frac{2}{\tau_e}. \tag{42}$$

Further substituting (30) and (40) into $1/\tau_w = 2/\tau_e$, and using $\Delta t_- \approx \Delta t$, we get an expression for l_c:

$$l_c \sim u_c \Delta t \sim \frac{(\mu_* \pi)^2}{\varepsilon}. \tag{43}$$

Combining (38) and (43), and eliminating μ_*, we get:

$$l_c \sim \frac{l_m}{1+\varepsilon l_m/2} \approx \begin{cases} l_m, & \varepsilon l_m \ll 1, \\ 2/\varepsilon, & \varepsilon l_m \gg 1. \end{cases} \tag{44}$$

Equation (44) shows that for small l_m where the cold pool is weak, little trigger effect is needed to balance the relatively weak mixed layer damping process, so the cloud spacing approaches the maximum cold pool size predicted by Romps and Jeevanjee (2016). For large l_m, the cloud spacing is constrained by cold pool fractional entrainment rate. The mixed layer damping is strong, so the trigger also needs to be strong. This enhances the incomplete recovery, and therefore l_c approaches an asymptotic value of $2/\varepsilon$, which significantly deviates from l_m. This prediction is compared to LES in section 3.

3. Comparison with LES

a. Simulation setup

In this section, we use LES to benchmark the cloud spacing theory. As an application, we attempt to explain why increasing the rain evaporation rate leads to a larger cloud spacing, as has been reported by Nissen and Haerter (2021).

We make a series of LES with the Bryan Cloud Model 1 (CM1, Bryan and Fritsch 2002) to study how the cloud spacing depends on the rain evaporation rate. The experimental method closely follows Nissen and Haerter (2021). The control run is an LES of deep convection over a uniform sea surface temperature of 300 K and zero Coriolis parameter in a 96×96 km^2 doubly periodic square domain. The mesh is $480 \times 480 \times 130$, with a uniform horizontal grid spacing of 200 m, and a vertically nonuniform grid with 15 grid points within the lowest 1 km. The model uses the simple planetary boundary layer scheme of Bryan and Rotunno (2009), the surface layer model of Jiménez et al. (2012), the RRTMG radiation transfer scheme (Clough et al. 2005) (with the zenith angle fixed at 50.5° and the solar constant reduced to 650.83 W m^{-2}, following Bretherton et al.

(2005)), and Morrison double-moment microphysics scheme (Morrison et al. 2005). We initialize the model with a radiative-convective equilibrium (RCE) state sounding, from the horizontally averaged water vapor mixing ratio and potential temperature profiles of a 120×120 km^2 cloud-permitting simulation with 2 km horizontal resolution at the end of day 100. This sounding is the same as that used by Fu and O'Neill (2021a).

For the control run, Fig. 6a shows that the domain-averaged precipitable water (PW) oscillates within the first 2 days and then slowly climbs. This indicates that the coarse-resolution initialization still deviates from the RCE state of the high-resolution LES setup. However, both the standard deviation of PW (Fig. 6b) and the diagnosed cloud spacing (Fig. 6c, which will be introduced shortly) do not systematically change after two days. This two-day time scale should be the adjustment time of boundary layer quasi-equilibrium (Raymond 1995). The above evidence indicates that it should be sufficient to investigate cloud spacing (a 10^1-10^2 km mesoscale phenomenon) in a boundary layer quasi-equilibrium state, without requiring the stricter RCE, which has an adjustment time scale of $\sim$ 15 days needed for moist static energy to vertically mix across the troposphere (Tompkins and Craig 1998). In addition, the long RCE adjustment time is hard to meet in the real atmosphere at the mesoscale which continuously evolves (Mapes 1997). Thus, we have not spent the extra effort to run in a strict RCE state, and we will refer to "equilibrium" as boundary layer quasi-equilibrium unless further noted.

We performed 12 experiments where the inverse of rain evaporation timescale (parameter EPSR in "morrison.F" file) is multiplied by a constant coefficient E_v, with $E_v = 0.15$, 0.2, 0.3, 0.4, 0.5, 0.6, 0.8, 1.0, 1.2, 1.5, 1.8, and 2.0 for EXP 1-12. The $E_v = 1.0$ test is the control run. First, we compare the flow pattern of different tests. At day 4 when the equilibrium state is reached, there is a visible increase of cold pool size and therefore cloud spacing as E_v increases (Figs. 7 and 8), in agreement with the LES of Nissen and Haerter (2021). For the 12 tests, no convective self-aggregation (CSA) is observed within the first 5 days. This is different from Nissen and Haerter (2021) who observed a clear convective self-aggregation pattern by day 2 in their $E_v = 0.1$ and 0.2 tests. In an additional $E_v = 0.1$ test we performed (not shown), there is indeed a signal of CSA on the flow pattern at day 5.

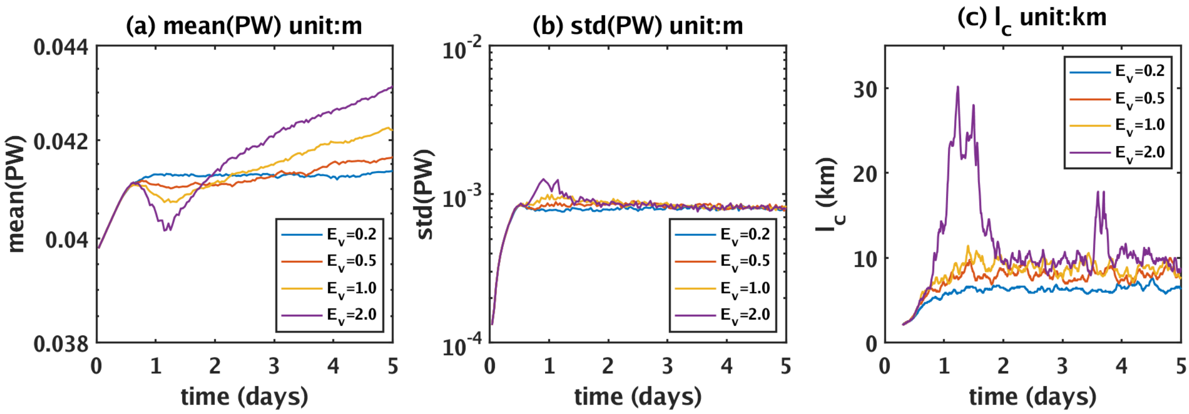

FIG. 6. (a) The time evolution of domain-averaged column precipitable water (unit: m) for $E_v = 0.2$ (blue line), $E_v = 0.5$ (red line), $E_v = 1.0$ (yellow line), and $E_v = 2.0$ (purple line). (b) is the same as (a), but for the standard deviation of column precipitable water with a logarithmic ordinate. (c) is the same as (a), but for the time evolution of cloud spacing l_c. The l_c is diagnosed as the spatial autocorrelation lag of the mixed layer water vapor content that first crosses 0.1 from above. Due to the quasi-isotropy of the pattern, a 1D x-direction profile is extracted from the 2D autocorrelation function to calculate the lag. The overshooting of l_c for the $E_v = 2.0$ test between day 3.5 and day 4 is an intermittent event that needs further investigation.

b. The qualitative feature of cloud spacing

The cloud spacing is calculated as twice the spatial autocorrelation lag of the mixed layer vapor content (vertically averaged within the lowest 551 m) that crosses an autocorrelation value of 0.1 from above for the first time (Fig. 9a). This choice roughly corresponds to the opposite phase lag, which has been quantified with the minimum point of the spatial autocorrelation function by Haerter et al. (2017). We do not adopt that approach because the autocorrelation function fluctuates too much at a large lag to work reliably. In addition, they used the mixed layer vapor convergence rate instead, which does not work as well as the mixed layer vapor content for our data.

Figure 10 shows that the diagnosed l_c indeed increases with E_v, but the increasing rate is lower in the log-log scale for a higher E_v. This flattening trend qualitatively agrees with figure 2B of Nissen and Haerter (2021), though they only have four different E_v tests ($E_v = 0.1, 0.2, 0.6, 1.0$). They used a delicate gust front tracking method to diagnose the cold pool radius at large cold pool age, which is considered to be close to our l_c based on spatial autocorrelation. Their figure 2B

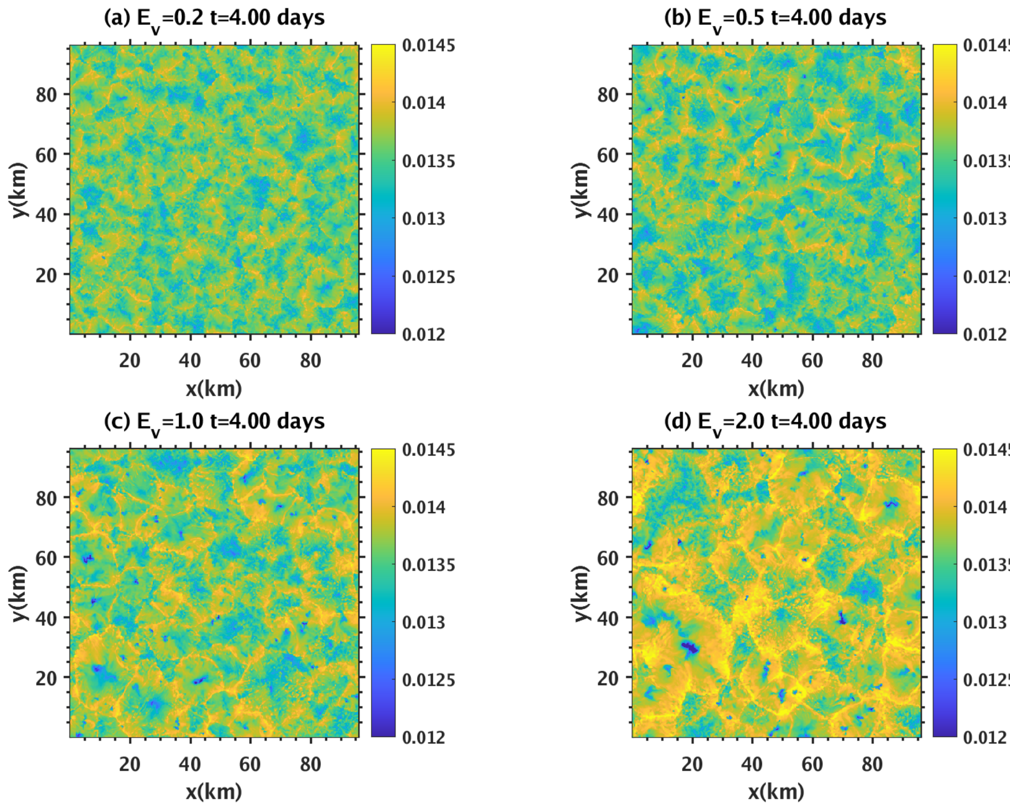

FIG. 7. The mixed layer water vapor mixing ratio (vertically averaged within the lowest 551 m level) at day 4. (a)-(d) denote $\mathrm{E_v} = 0.2$, 0.5, 1.0, and 2.0 tests. This quantity is used to diagnose cloud spacing l_c.

shows that the l_c grows steadily between their $\mathrm{E_v} = 0.1$, 0.2 and 0.6 tests, but remains roughly the same for their $\mathrm{E_v} = 0.6$ and $\mathrm{E_v} = 1$ tests. They commented on the monotonic growth trend, but did not mention the insensitivity to $\mathrm{E_v}$ reflected by the $\mathrm{E_v} = 0.6$ and $\mathrm{E_v} = 1$ tests. Our theory (section 2d) predicts that l_c increases with l_m, and approaches an upper bound of $2/\varepsilon$ for a large l_m. Can we derive a l_c-$\mathrm{E_v}$ relation based on the l_c-l_m relation (44)? The key is to understand how the fully dissipated cold pool radius l_m depends on $\mathrm{E_v}$. Based on the RJ16 model of l_m (2), this requires an understanding of how V_0, $(\theta_{ml} - \theta_{ini})$, and $(\theta_{surf} - \theta_{ini})$ depend on $\mathrm{E_v}$ or l_c itself.

c. A quantitative prediction of cloud spacing

We present some novel findings on how $\mathrm{E_v}$ influences updrafts, downdrafts, and subsequently cold pools, which are the basis for understanding the l_c-$\mathrm{E_v}$ relation.

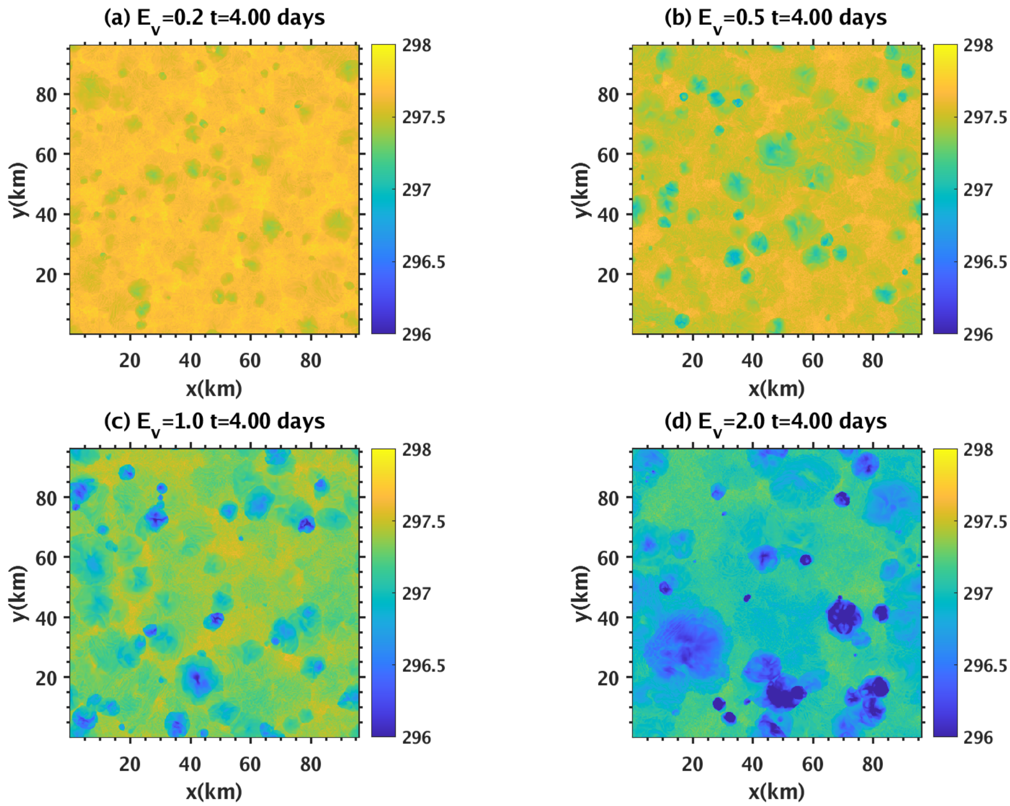

FIG. 8. The same as Fig. 7, but for z = 12.5 m (near-surface) potential temperature.

First, we analyze the updraft statistics. Figure 10 shows that the magnitude of updraft radius l_0 is approximately $1/5$ of l_c, though the exact scaling with respect to $\mathrm{E_v}$ is different. Its diagnostic method is illustrated in Fig. 9b. The updraft speed w_u (Fig. 11a) does not increase with l_0. This differs from the previous finding that a wider cloud has a stronger updraft, which is explained as a better protected convective core (Khairoutdinov et al. 2009; Schlemmer and Hohenegger 2014). The origin of the difference needs further investigation. Based on this phenomenon, we consider the cloud dissipation in the updraft phase to be insensitive to $\mathrm{E_v}$ and therefore temporarily ignore the convective entrainment feedback (wider cold pools lead to stronger updrafts) in the cloud spacing theory.

Second, we analyze the downdraft and cold pool statistics. Because updraft speed is insensitive to $\mathrm{E_v}$, the rain evaporation rate should be proportional to $\mathrm{E_v}$. The downdraft velocity increases slightly with $\mathrm{E_v}$ for $\mathrm{E_v} \lesssim 0.4$, but increases steeply with $\mathrm{E_v}$ with an ${\mathrm{E_v}}^{1/3}$ slope for $\mathrm{E_v} \gtrsim 0.4$ (Fig. 11a). We explain this transition behavior of downdraft velocity as the water loading effect: for

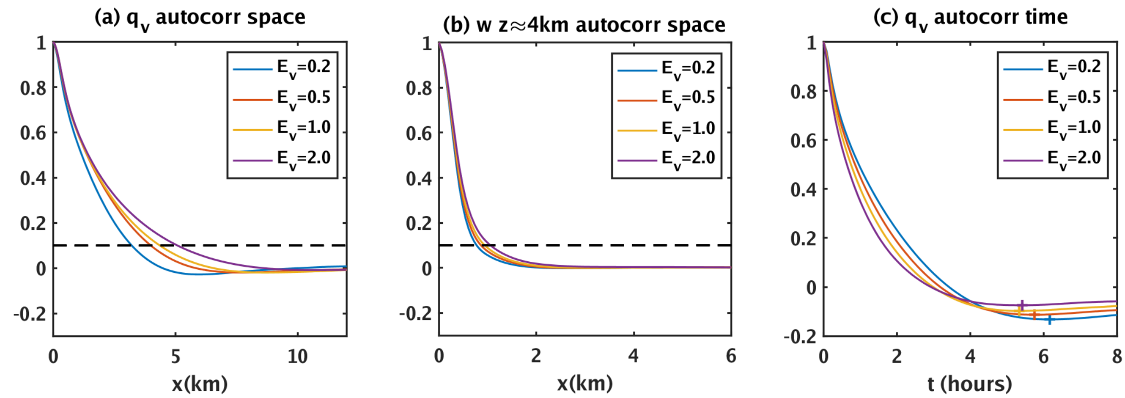

FIG. 9. (a) The temporally averaged (a two-day-long time series between day 3 and day 5) spatial autocorrelation of the mixed layer vertically averaged water vapor content for $\mathrm{E_v} = 0.2$ (blue line), $\mathrm{E_v} = 0.5$ (red line), $\mathrm{E_v} = 0.7$ (yellow line), and $\mathrm{E_v} = 1.0$ (purple line). There is an additional dashed black line denoting the 0.1 autocorrelation value that is used to diagnose cloud spacing in Figs. 6c and 10. (b) The same as (a), but for the vertical velocity at $z \approx 4$ km. (c) The detrended temporal autocorrelation of the mixed layer vapor content, using a two-day-long time series between day 3 and day 5. The curve is averaged over the 480×480 grid points. The "+" signs with the corresponding colors denote the minimum value points that are plotted in Fig. 12b.

$\mathrm{E_v} \lesssim 0.4$, the rainwater loading is a significant driving force of the downdraft, which does not change with $\mathrm{E_v}$.

We have not performed gust front tracking (e.g. Torri and Kuang 2019; Nissen and Haerter 2021), so the value of the mean gust front speed u_c is unknown. However, both the mean and standard deviation of surface total wind increase with ${\mathrm{E_v}}^{1/3}$ (Fig. 11b). Based on this, we predict that $u_c \sim {\mathrm{E_v}}^{1/3}$. We use dimensional analysis to explain the ${\mathrm{E_v}}^{1/3}$ scaling of the downdraft speed and surface wind. Equation (10) shows that the gust front speed u_c depends on the evaporation-induced buoyancy anomaly of a downdraft b_d and cold pool height H_c: $u_c \sim (b_d H_c)^{1/2}$. We assume b_d depends on the evaporation-induced buoyancy loss rate in a downdraft Q (unit: m s^{-3}), as well as the mixed layer height H_m. We choose Q because $Q \propto \mathrm{E_v}$. We choose H_m because Torri and Kuang (2016) found that most cold pool air comes from the mixed layer top. Dimensional analysis yields:

$$b_d \sim Q^{2/3} H_m^{1/3} \quad \Rightarrow \quad u_c \sim b_d^{1/2} \sim Q^{1/3} \sim {\mathrm{E_v}}^{1/3}. \tag{45}$$

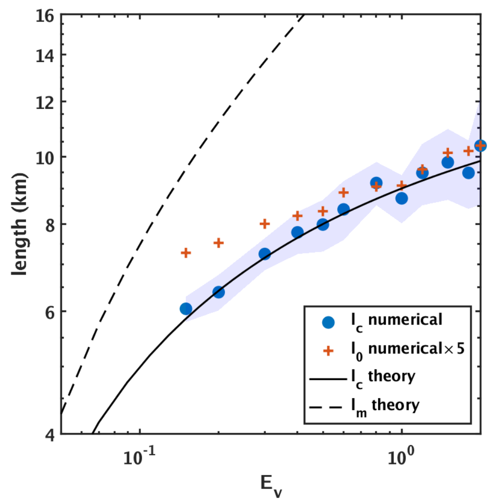

Fig. 10. Some length quantities in log-log coordinate. The blue circle denotes the l_c diagnosed from the LES. The cloud spacing is diagnosed from individual snapshots first and then temporally averaged over a two-day-long time series between day 3 and day 5. The time series correspond to the curves in Fig. 6c. The blue shadow denotes the ± 1 standard deviation range of the cloud spacing time series. The red "+" denotes the updraft radius l_0 diagnosed from the LES, multiplied by five. The method is the same as diagnosing l_c, but the physical variable is vertical velocity at $z \approx 4$ km height. The solid black line is the theoretical prediction of (49), using $\beta = 3$ and $\Phi_0 = 2.5$. The dashed black line denotes the theoretical l_m, which is calculated with $l_m = \Phi_0 \mathrm{E_v}^{2/9} l_c$.

Physically, the $b_d \sim Q^{2/3} \sim \mathrm{E_v}^{2/3}$ scaling, which is confirmed in Fig. 11c by linking b_d to the standard deviation of near-surface potential temperature, comes from the argument that b_d is determined by the product of the evaporative cooling rate Q and the residence time of a parcel in the rain shaft $(H_m/b_d)^{1/2}$. Because a larger Q leads to a faster downdraft ($w_d \sim (b_d H_m)^{1/2} \sim u_c$) and therefore a shorter residence time, b_d grows with Q more slowly than linearly. One might be curious why there is $u_c \sim \mathrm{E_v}^{1/3}$ even for $\mathrm{E_v} \lesssim 0.4$, where the water loading is an important additional acceleration that shortens the parcel residence time in the downdraft and should make u_c smaller than the $\mathrm{E_v}^{1/3}$ scaling. We have not figured out a rigorous explanation, but we speculate that the dynamical acceleration on the cold pool due to water loading could make it unstable to Kelvin-Helmholtz instability and therefore lead to enhanced vertical mixing (e.g. Lee et al. 1974; Turner 1986). The mixing, which should occur near the downdraft site, might make some cold pool air return to the downdraft and be further cooled. We leave a careful investigation for future work.

Third, we analyze $(\theta_{ml} - \theta_{ini})$ and $(\theta_{surf} - \theta_{ini})$. Figure 8d shows that the difference between the potential temperature of an initial cold pool and the sea surface temperature $(\theta_{surf} - \theta_{ini})$ roughly increases from 2.5 K to 3.7 K as $\mathrm{E_v}$ increases from 0.2 to 2.0, where $\theta_{surf} = 300$ K is the prescribed sea surface temperature. Note that the relationship between $(\theta_{surf} - \theta_{ini})$ and $\mathrm{E_v}$ is not a power law: $(\theta_{surf} - \theta_{ini})$ asymptotically approaches a 2 K base value as $\mathrm{E_v} \to 0$. Such a temperature difference is needed to support the basic boundary layer heat flux. The difference $(\theta_{ml} - \theta_{ini})$, which is measured by the near-surface potential temperature's standard deviation and denotes the buoyancy anomaly, increases from roughly 0.07 K to 0.3 K as $\mathrm{E_v}$ increases from 0.2 to 2.0 (Fig. 11c) and obeys $(\theta_{ml} - \theta_{ini}) \sim \mathrm{E_v}^{1/3}$. Thus, we consider the change of $(\theta_{ml} - \theta_{ini})$ to dominate the change of $(\theta_{ml} - \theta_{ini})/(\theta_{surf} - \theta_{ini})$, which is considered to approximately obey $\mathrm{E_v^{1/3}}$.

With the above preparations, we derive the expression of $V_0(\theta_{ml} - \theta_{ini})/(\theta_{surf} - \theta_{ini})$ and then l_m. The cold pool formation is a continuous cold air production process, while the RJ16 model considers it as an initial value problem of cold air collapse. To fill the gap, we consider V_0 to be the total amount of air that has entered the downdraft in a convective event, which is proportional to the total rain evaporation amount in a cylindrical rain shaft:

$$V_0(\theta_{ml} - \theta_{ini}) \sim \mathrm{E_v} l_0^2 \Delta t_+. \tag{46}$$

Here Δt_+ is the convective duration time that has been introduced in section 2, and the height of the evaporation cylinder H_m is considered to be independent of $\mathrm{E_v}$. Equation (46) can be alternatively derived by separately estimating V_0 and $(\theta_{ml} - \theta_{ini})$. Suppose $V_0 \sim \pi l_0^2 w_d \Delta t_+$, which is the volume of air that passes the cylinder top. Using the confirmed scaling $w_d \sim \mathrm{E_v}^{1/3}$ (Fig. 11a, not considering the complexity brought by water loading) and $\theta_{ml} - \theta_{ini} \sim \mathrm{E_v}^{2/3}$ (Fig. 11c), we also arrive at (46).

The individual cloud statistics (l_0 and Δt_+) can be linked to the cloud population statistics (l_c and Δt) by introducing a domain mean updraft mass flux M_u:

$$M_u \equiv \rho \underbrace{\frac{\Delta t_+}{\Delta t} \frac{l_0^2}{l_c^2}}_{\alpha_+} w_u, \tag{47}$$

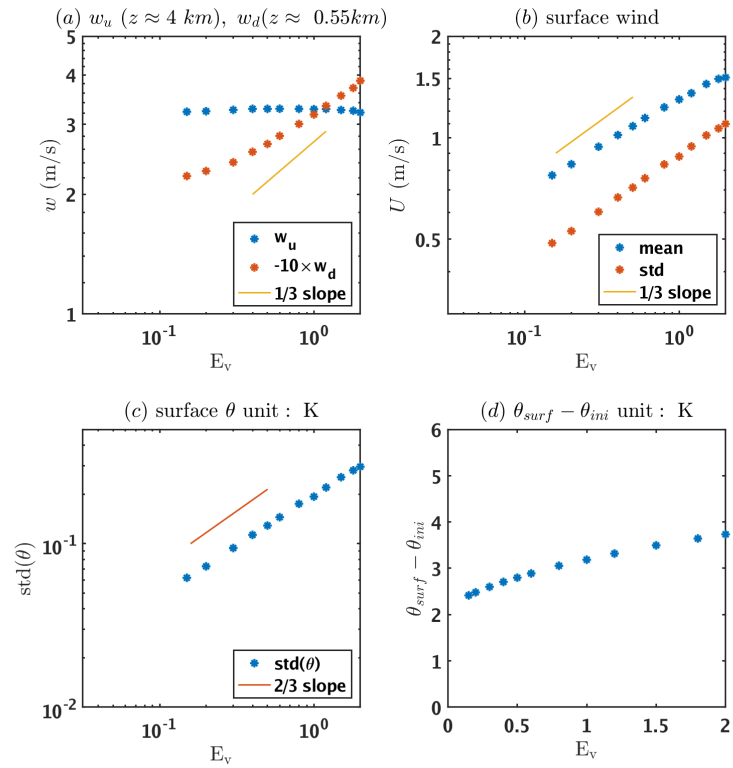

FIG. 11. Some updraft, downdraft, and mixed layer statistics calculated with the data between day 3 and day 5. All plots except (d) use log-log coordinate. (a) The blue “*" denotes the dependence of updraft speed w_u at around 4 km height on the evaporation rate ratio E$_v$. A grid point is identified as an updraft grid point if the cloud liquid water content is above 10^{-5} kg kg^{-1} and the vertical velocity is above 1 m s^{-1}, following Romps and Kuang (2010). The red “*” denotes the mean downdraft speed magnitude w_d at around 551 m height, which is near the mixed layer top. A grid point is identified as a downdraft grid point if the rainwater content is above 10^{-5} kg kg^{-1} and the vertical velocity is negative, which is a modification from the “broad" criteria of downdraft by Torri and Kuang (2016). Their minimum rainwater criterion is zero, in contrast to our 10^{-5} kg kg^{-1} . The yellow line denotes a reference ${E_v}^{1/3}$ power law slope. (b) The E$_v$ versus the average value (blue “*”) and standard deviation (red “*”) of surface total wind ($z = 12.5$ m level). The yellow line denotes a reference for ${E_v}^{1/3}$ power law slope. (c) The E$_v$ versus the standard deviation of near-surface potential temperature. The red line denotes a reference for ${E_v}^{2/3}$ power law slope. (d) The E$_v$ versus $\theta_{surf} - \theta_{ini}$, which is diagnosed as the difference between the sea surface temperature (300 K) and the mean $z = 12.5$ m potential temperature in the downdraft region.

where ρ is air density and α_+ is updraft fractional area. Figure 12a shows that between day 3 and day 5, α_+ is insensitive to $\mathrm{E_v}$ for $\mathrm{E_v} \lesssim 0.3$, and increases slightly with $\mathrm{E_v}$ for $\mathrm{E_v} \gtrsim 0.3$ with a $\alpha_+ \sim \mathrm{E_v}^{1/12}$ scaling. We qualitatively explain the increase of α_+ and therefore M_u as the enhanced surface heat flux in a higher $\mathrm{E_v}$ case where the surface wind is stronger (Fig. 11b). The enhanced surface heat flux must either be balanced by a stronger radiative cooling in the mixed layer interior, or a stronger radiation- and precipitation-driven downdraft mass flux whose sum equals to the updraft mass flux (Raymond 1995; Emanuel and Bister 1996). We expect the α_+-$\mathrm{E_v}$ relation to slowly evolve as the system approaches a radiative-convective equilibrium state, and leave the quantitative prediction of the α_+-$\mathrm{E_v}$ relation for future work. Because the $1/12$ slope is very flat, we assume α_+ to be independent of $\mathrm{E_v}$ in deriving the cloud spacing theory. This yields $\Delta t_+ l_0^2 \sim \alpha_+ \Delta t l_c^2 \sim \Delta t l_c^2$.

The temporal autocorrelation is used to diagnose the convective period Δt (Fig. 12b). The minimum temporal autocorrelation lag is considered to be related to a half convective cycle $\Delta t/2$, as is illustrated in Fig. 9c. Unfortunately, it does not converge for a time series as long as 2 days, with the minimum autocorrelation time interval growing as the length of the time series increases. This long-time memory manifests the deviation from an idealized oscillator and needs further investigation. Thus, we should not take the diagnosed minimum autocorrelation value to be the absolute value of $\Delta t/2$, but it might be useful as a relative value. One robust feature is that the minimum autocorrelation time slightly drops as $\mathrm{E_v}$ increases. Figure 12c confirms that Δt obeys $\Delta t \sim l_c/u_c$ scaling.

Substituting $\Delta t \sim l_c/u_c$ and $\Delta t_+ l_0^2 \sim \alpha_+ \Delta t l_c^2$ into (46), and then into (2), we get:

$$l_m \sim [V_0(\theta_{ml} - \theta_{ini})]^{1/3} \sim \left(\mathrm{E_v} \alpha_+ \Delta t l_c^2\right)^{1/3} \sim \mathrm{E_v}^{2/9} l_c. \tag{48}$$

Equation (48) predicts that as the hydrometeor evaporation rate increases, l_c deviates more from the maximum cold pool length l_m, so convection manifests as a more forced and less spontaneous event. To get a quantitative l_c-$\mathrm{E_v}$ relation, we express l_m as $l_m = \Phi_0 \mathrm{E_v}^{2/9} l_c$, where Φ_0 is a larger-than-unity nondimensional free parameter that equals to l_m/l_c when $\mathrm{E_v} = 1$. Another nondimensional free parameter is β which re-expresses (44) as $l_c = l_m/(1 + \varepsilon l_m/\beta)$. The β replaces the factor of 2 in (44), because the factor comes from the sinusoidal wave assumption in estimating the cutoff induced damping rate $1/\tau_{cut}$ (36) which is very qualitative. Thus, β/ε is a predicted universal upper bound of l_c. Combining the modified (44) and modified (48), we get:

$$l_c = \frac{\beta}{\varepsilon}\left(1 - \Phi_0^{-1}{\mathrm{E_v}}^{-2/9}\right). \tag{49}$$

Using $\beta = 3$ and $\Phi_0 = 2.5$, we get a good match between the theory and the LES result (Fig. 10). We make two remarks:

- This derivation assumes $\alpha_+ \sim {\mathrm{E_v}}^0$. The $-2/9$ exponent will be modified if a different α_+-$\mathrm{E_v}$ relation is used.
- The model predicts l_m to be at least 1.5 times of l_c for our 12 tests (Fig. 10). This indicates that the $t' \ll \Delta t_-$ requirement for deriving the cloud spacing theory (44) is not well satisfied. Thus, it is safer to say that the model qualitatively predicts the increase and stagnancy of l_c with increasing $\mathrm{E_v}$.

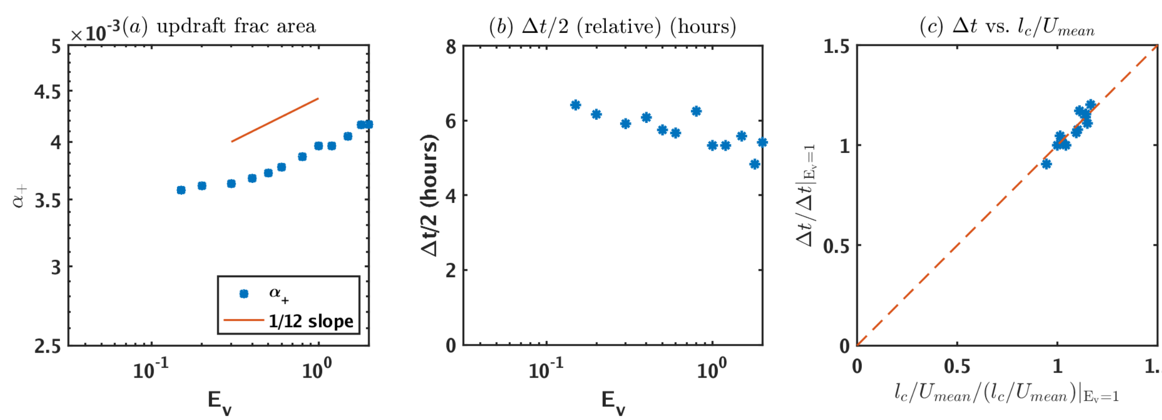

FIG. 12. Some cloud population statistics calculated with the data between day 3 and day 5. (a) The "*" denotes the dependence of updraft fractional area α_+ on the rain evaporation rate ratio $\mathrm{E_v}$ in a log-log coordinate. The solid line is a ${\mathrm{E_v}}^{1/12}$ slope reference. (b) The dependence of convective half-period $\Delta t/2$ on $\mathrm{E_v}$. The $\Delta t/2$ corresponds to the minimum lag of the composite temporal autocorrelation function which is calculated in the same way as in Fig. 9c. Note that the diagnosed $\Delta t/2$ increases with the time series length, so only the relative magnitude between different $\mathrm{E_v}$ tests is useful. (c) The "*" denotes the relation between Δt and l_c/U_{mean}, where U_{mean} is the domain-averaged surface total wind ($z = 12.5$ m level). In the plotting, Δt, l_c and U_{mean} are normalized with their value at $\mathrm{E_v} = 1$. The dashed line is a 1-to-1 reference line.

4. Summary and conclusion

This paper presents a theory of cloud spacing for homogeneous and quasi-equilibrium deep convection, which involves precipitation. We propose a new perspective: precipitating convection with gust front can be viewed as a hydrodynamic instability problem, with the cloud distribution pattern being determined by the most unstable mode. A novel piecewise linear oscillator model is built to depict the primary oscillation, which consists of a long recovery phase associated with the cold pool and a short convective phase associated with updrafts and downdrafts. The fact that the cold pool triggers new convection before it completely recovers inspires us to add a cutoff to the oscillator: the recovery phase ends before the cold pool velocity returns to zero, which is shown to be a damping effect. If the recovery phase ends too early, the mixed layer moisture recovery will be insufficient. If the recovery phase ends too late, the cold pool lifting effect will be too weak. This trade-off leads to an optimal cloud spacing l_c (the most unstable mode), which is expressed as a deviation from the full recovery length of a cold pool (l_m) that already has a theory (Romps and Jeevanjee 2016). The deviation is determined by a parameter μ_* which denotes the downdraft production efficiency by gust front lifting. The μ_* is difficult to determine by directly considering the physics of triggering and downdraft production. However, the quasi-equilibrium assumption enables us to solve it with the other side of the convective life-cycle. The oscillator serves as a hub that puts the amplifying and damping effects in the convective and recovery phase together. They include:

- The amplifying effect of 1) gust front lifting and 2) convective instability due to precipitation delay.
- The damping effect of 3) cold pool incomplete recovery, 4) cold pool entrainment, and 5) updraft drag.

In the appendix, we surmise (without rigorous proof) that the convective instability and updraft drag should largely cancel each other if the updraft thermals are in a force balance between buoyancy and drag as has been proposed by Romps and Charn (2015). The rest of the three effects should make the most unstable mode neutral, which provides an additional independent relation between l_c and μ_*. Combining the trade-off constraint and the neutral constraint, we eliminate μ_* and get a theory of l_c. It shows that when the cold pool is weak, l_c follows the maximum length l_m. When the cold pool is strong, l_c asymptotically approaches an upper bound which is proportional to the inverse of the cold pool fractional entrainment rate ε.

A series of LES are performed to benchmark the theory of cloud spacing. In the microphysics scheme, the inverse of rain evaporation timescale is modified to $\mathrm{E_v}$ times of the original value. We studied the dependence of the updraft and the mixed layer statistics on $\mathrm{E_v}$ and used them to establish a relationship between the theoretically predicted l_m and $\mathrm{E_v}$. The l_c is diagnosed with the spatial autocorrelation of the mixed layer water vapor content. An initial 2-day spin-up time is needed for the mixed layer to enter a quasi-equilibrium state and for the l_c value to stabilize, without the need for a full radiative-convective equilibrium. The theory successfully predicts the increase and stagnancy of l_c with increasing $\mathrm{E_v}$.

More LES investigations by changing other parameters (e.g. rain terminal fall velocity, radiative cooling rate) are needed to further benchmark the theory. Given the importance of ε in our theory, a natural question to ask is what determines ε (e.g. Turner 1986), especially the role of rainwater loading near the downdraft that should influence the Froude number there. Whether our LES has sufficient horizontal resolution (currently 200 m) to describe the entrainment process is also an important question.

An extension to equilibrium convection over constant surface heat flux boundary condition is considered for future work, which is important for understanding the role of background wind. Simulations showed that a characteristic cloud spacing also exists in that scenario (Böing et al. 2012; Gentine et al. 2016). For the interactive surface flux case, the gust front can collect a large amount of wind-intensified heat flux and fuel the updraft (Langhans and Romps 2015). In addition, it is the interactive surface heat flux boundary condition that makes $1/\tau_{cut} \sim t'^2$, which leads to the convexity of this optimization problem. For the constant-flux case, surface heating rate is uniform in the calm non-cold pool region and the windy cold pool region. Thus, the recovery of the non-cold pool region may play a more important role than the interactive surface flux case. Because the recovery in the non-cold pool region is likely primarily due to near-equilibrium boundary layer convective cells, we expect an exponential relaxation, which might provide the convexity needed for the optimization problem.

The theory has many potential applications:

- Knowledge of cloud spacing tells us how the total convective mass flux distributes in each cloud. It is a measure of convective intermittency that has been shown to significantly influence the stochastic vorticity accumulation process in tropical cyclogenesis (Fu and O'Neill 2021a; Fu and O'Neill 2021b).
- The cloud spacing theory can be extended to include unsteady effect which is important in the real atmosphere that has diurnal cycle and synoptic wave (Garg et al. 2021). In particular, it might be extended to study shallow-to-deep convection transition which involves positive feedback between convective deepening and cold pool widening (Böing et al. 2012; Schlemmer and Hohenegger 2014; Haerter et al. 2020).
- In a follow-up paper, this single cloud model is updated to an array clouds that interact with each other via cold pools. The new model will provide insights on the spread of convective activity in an inhomogeneous state, which is vital for understanding the early stage of convective self-aggregation and tropical cyclogenesis.

Acknowledgments. We are grateful to Dr. Junfei Li at Duke University, Dr. Zhihong Tan at Princeton University, and Prof. Zhaohua Wu at Florida State University for helpful discussion. We thank Prof. Bowen Zhou at Nanjing University for inspiring the first author to think about the equilibrium precipitating convection problem many years ago. We thank Stanford Research Computing Center for providing the computational resource.

Data availability statement. A derivation note, movies of the LES (the movie version of Figs. 7 and 8), the CM1 namelist file, as well as all the figure plotting codes can be downloaded at: https://stanford.box.com/s/lab3jv2cd8nm7o7xjvff2pf5c4vm28dt . The LES data can be obtained by contacting the corresponding author.

APPENDIX

The potential balance between updraft drag and precipitation delay in the oscillator

In this appendix, we start from the vertical momentum equation of the updraft (w_u) to show that precipitation delay is a manifestation of convective instability, which induces updraft drag to balance it. A linear analysis is performed for the case where the precipitation delay τ_p is much smaller than the convective duration time Δt_+.

The precipitation delay denotes the delay of rainfall to updraft,which is the time needed for rain to form and fall to the mixed layer (Emanuel 1994). Because downdraft is produced by rain evaporation, we consider precipitation delay to denote the delay of downdraft to updraft. We denote the delay time as τ_p. Letting w_u be the updraft strength and χ be the ratio of downdraft strength to updraft strength, we get a kinematic relation:

$$w_d = \chi w_u(t - \tau_p). \tag{A1}$$

The χ depends on the rain formation efficiency and sub-cloud rain evaporation rate (Emanuel et al. 2014; Lutsko and Cronin 2018; Fu and Lin 2019).

The vertical momentum equation for the updraft is:

$$\frac{\partial w_u}{\partial t} = g\frac{\theta'_e}{\theta_0} \underbrace{-\frac{1}{\rho_0}\frac{\partial p'}{\partial z} - \varepsilon_u w_u^2}_{\approx -w_u/\tau_{d+}}, \tag{A2}$$

where $\theta_0 = 300$ K is a reference potential temperature, $\rho_0 = 1$ kg m^{-3} is a reference air density, p' is the perturbation pressure, and ε_u is the updraft fractional entrainment rate (unit: m^{-1}). Here w_u denotes a column-averaged value, and θ'_e denotes the mixed layer equivalent potential temperature anomaly that represents the potential temperature anomaly within the updraft. Romps and Charn (2015) showed that the pressure gradient term can be expressed in the drag form:

$$-\frac{1}{\rho_0}\frac{\partial p'}{\partial z} \approx -\eta C_D w_u^2, \tag{A3}$$

where η is a coefficient with a unit of m^{-1}, and C_D is the nondimensional drag coefficient. The gust front lifting is a low-level pressure anomaly (Jeevanjee and Romps 2015) which is not included here and will be left for future investigation. Equation (A3) inspires us to express the bulk damping due to drag and entrainment as a constant damping time scale τ_{d+}, as is marked in (A2). In addition, we get an expression of γ_+ by comparing (A2) with (4):

$$\gamma_+ = \frac{g}{\theta_0}\chi. \tag{A4}$$

Next, we study the role of precipitation delay, and limit our discussion to the convective phase ($0 < t < \Delta t_+$). Consider a normal mode solution of w_u and θ'_e:

$$w_u = \mathrm{Re}\left\{A_{w_u} e^{-i\omega_+ t}\right\}, \quad \theta'_e = \mathrm{Re}\left\{A_{\theta_e} e^{-i\omega_+ t}\right\}, \tag{A5}$$

where Re{} denotes taking the real part, ω_+ is the complex frequency for the convective phase, A_{w_u} is the complex amplitude of w_u, and A_{θ_e} is the complex amplitude of θ'_e. The ω_+ deviates from the primary oscillation frequency $\Omega_+ = \pi/\Delta t_+$, which is real. Equation (A5) indicates that (A1) can be rewritten as:

$$w_d = \chi A_{w_u} e^{-i\omega_+(t-\tau_p)} \approx \chi w_u e^{i\Omega_+\tau_p}, \tag{A6}$$

where we have assumed τ_p to be much smaller than Δt_+ to guarantee $e^{i\omega_+\tau_p} \approx e^{i\Omega_+\tau_p}$. Substituting (A5) and (A6) into (3) and (A2), we get a complex oscillation equation:

$$\frac{d^2 w_u}{dt^2} + \omega_+^2 w_u = 0, \tag{A7}$$

with

$$\omega_+ = \left(\frac{\gamma_+\alpha_+\Delta\theta_e}{H_c}\right)^{1/2} e^{i\frac{\Omega_+\tau_p}{2}} = \Omega_+\left[\cos\left(\frac{\Omega_+\tau_p}{2}\right) + i\sin\left(\frac{\Omega_+\tau_p}{2}\right)\right]. \tag{A8}$$

Equation (A8) indicates that the precipitation delay extends the convective time and makes the system unstable. The growth rate due to the delay is measured with a time scale $\tau_{\Delta+}$ which obeys:

$$\frac{1}{\tau_{\Delta+}} = \Omega_+ \sin\left(\frac{\Omega_+\tau_p}{2}\right). \tag{A9}$$

The amplification rate increases with the delay time. Physically, the delay is a destabilizing factor because it provides time for the updraft to self-amplify without being influenced by the downdraft. This is a manifestation of basic convective instability.

How does the delay-induced convective instability compare with the stabilizing effect of the updraft drag? Romps and Charn (2015) found that an individual thermal in moist convection reaches a "terminal velocity" due to the balance between buoyancy and drag, with little contribution from entrainment and detrainment. Our w_u equation (A2) denotes an ensemble of thermals at different stages, so we do not expect $\partial w_u/\partial t$ to diminish. One heuristic way to apply the finding by Romps and Charn (2015) to an updraft plume is to consider the time integration of the buoyancy and the damping term within the convective phase be zero:

$$\int_0^{\Delta t_+} \frac{\partial w_u}{\partial t} dt = \int_0^{\Delta t_+} g\frac{\theta_e'}{\theta_0} dt - \frac{1}{\tau_{d+}} \int_0^{\Delta t_+} w_u dt \approx 0, \tag{A10}$$

which is based on (A2). If there is no precipitation delay, the integral of the buoyancy term will be zero (e.g. Fig. 4), which means no net destabilizing effect. Using (3) and the normal mode form (A5), we express the time integral of θ_e' as:

$$\begin{aligned}\int_0^{\Delta t_+} \theta_e' dt &= \int_0^{\Delta t_+} \int \frac{\partial \theta_e'}{\partial t} dt dt' \\ &\approx \chi |A_{w_u}| \frac{\alpha_+ \Delta\theta_e}{H_c} \frac{1}{\Omega_+} \int_0^{\Delta t_+} \cos\left[\Omega_+(t' - \tau_p)\right] dt' \\ &= \chi |A_{w_u}| \frac{\alpha_+ \Delta\theta_e}{H_c} \frac{1}{\Omega_+^2} 2\sin(\Omega_+ \tau_p).\end{aligned} \tag{A11}$$

Here we have used $w_u(t - \tau_p) \approx |A_{w_u}| \sin\left[\Omega_+(t - \tau_p)\right]$ in deriving the second line. The time integral of the updraft damping term is:

$$-\frac{1}{\tau_{d+}} \int_0^{\Delta t_+} w_u dt = -\frac{|A_{w_u}| \Delta t_+}{\tau_{d+}\pi} = -\frac{|A_{w_u}|}{\tau_{d+}\Omega_+}. \tag{A12}$$

Substituting (A11) and (A12) into (A10), and using the small delay assumption $\tau_p \ll \Delta t_+$, we get:

$$\tau_{\Delta+} = 4\tau_{d+}. \tag{A13}$$

This indicates that the time-averaged force balance corresponds to a time scale balance. Thus, we consider the buoyancy and damping effects to largely cancel each other in the convective phase of the oscillator, and therefore neglect both the precipitation delay and the damping on an updraft. Further investigations using LES that change the precipitation delay (e.g. by modifying the terminal fall velocity, Parodi and Emanuel 2009) are needed to verify this conclusion. One uncertainty is to what extent the force balance of individual thermals should work on an updraft plume which involves a chain of thermals (e.g. Morrison et al. 2020).

As a final remark, we comment on the difference between our precipitation delay and that used by the phenomenological shallow convection model of Koren and Feingold (2011) from which we get the inspiration. They modeled the accumulation of cloud water and its consumption by rain in a delayed differential equation. Koren et al. (2017) presented a linearized version of their model which shows the mathematical skeleton:

$$\frac{dq_c}{dt} = \underbrace{\frac{q_{ref} - q_c}{\tau_1}}_{\text{recovery}} - \underbrace{\lambda_p q_c(t - \tau_p)}_{\text{rain depletion}}. \tag{A14}$$

Here q_c is the cloud water content, q_{ref} is a reference cloud water content which is higher than q_c, τ_1 is a recovery time scale, and λ_p is a coefficient of rain depletion rate. The delay generates oscillation in this single prognostic variable model and could be a stable, neutral, or unstable factor. In contrast, our model uses a pair of thermodynamic-dynamical variables to represent the primary convective oscillation. Adding the precipitation delay only causes instability, which is shown to be a manifestation of convective instability that should be balanced by the drag on the updraft.

References

Böing, S. J., H. J. Jonker, A. P. Siebesma, and W. W. Grabowski, 2012: Influence of the subcloud layer on the development of a deep convective ensemble. *J. Atmos. Sci.*, **69 (9)**, 2682–2698.

Breidenthal, R., and M. Baker, 1985: Convection and entrainment across stratified interfaces. *J. Geophys. Res.*, **90 (D7)**, 13 055–13 062.

Bretherton, C. S., 1987: A theory for nonprecipitating moist convection between two parallel plates. part i: Thermodynamics and "linear" solutions. *J. Atmos. Sci.*, **44 (14)**, 1809–1827.

Bretherton, C. S., P. N. Blossey, and M. Khairoutdinov, 2005: An energy-balance analysis of deep convective self-aggregation above uniform sst. *J. Atmos. Sci.*, **62 (12)**, 4273–4292.

Bryan, G. H., and J. M. Fritsch, 2002: A benchmark simulation for moist nonhydrostatic numerical models. *Mon. Wea. Rev.*, **130 (12)**, 2917–2928.

Bryan, G. H., and R. Rotunno, 2009: The maximum intensity of tropical cyclones in axisymmetric numerical model simulations. *Mon. Wea. Rev.*, **137 (6)**, 1770–1789.

Chandrasekhar, S., 2013: *Hydrodynamic and hydromagnetic stability*. Courier Corporation.

Clough, S., M. Shephard, E. Mlawer, J. Delamere, M. Iacono, K. Cady-Pereira, S. Boukabara, and P. Brown, 2005: Atmospheric radiative transfer modeling: A summary of the aer codes. *J. Quant. Spectrosc. Radiat. Transf.*, **91 (2)**, 233–244.

Daleu, C. L., R. Plant, S. Woolnough, A. Stirling, and N. Harvey, 2020: Memory properties in cloud-resolving simulations of the diurnal cycle of deep convection. *J. Adv. Model. Earth Syst.*, **12 (8)**, e2019MS001 897.

Emanuel, K., A. A. Wing, and E. M. Vincent, 2014: Radiative-convective instability. *J. Adv. Model. Earth Syst.*, **6 (1)**, 75–90.

Emanuel, K. A., 1986: Some dynamical aspects of precipitating convection. *J. Atmos. Sci.*, **43 (20)**, 2183–2198.

Emanuel, K. A., 1994: *Atmospheric convection*. Oxford University Press on Demand.

Emanuel, K. A., and M. Bister, 1996: Moist convective velocity and buoyancy scales. *J. Atmos. Sci.*, **53 (22)**, 3276–3285.

Feingold, G., and I. Koren, 2013: A model of coupled oscillators applied to the aerosol–cloud–precipitation system. *Nonlinear Processes in Geophysics*, **20 (6)**, 1011–1021.

Feingold, G., I. Koren, H. Wang, H. Xue, and W. A. Brewer, 2010: Precipitation-generated oscillations in open cellular cloud fields. *Nature*, **466 (7308)**, 849–852.

Feng, Z., S. Hagos, A. K. Rowe, C. D. Burleyson, M. N. Martini, and S. P. de Szoeke, 2015: Mechanisms of convective cloud organization by cold pools over tropical warm ocean during the amie/dynamo field campaign. *J. Adv. Model. Earth Syst.*, **7 (2)**, 357–381.

Fielder, B. H., 1984: The mesoscale stability of entrainment into cloud-topped mixed layers. *J. Atmos. Sci.*, **41 (1)**, 92–101.

Fu, H., 2021: A linear stability analysis of two-layer moist convection with a saturation interface. *J. Fluid Mech.*, **928**.

Fu, H., and Y. Lin, 2019: A kinematic model for understanding rain formation efficiency of a convective cell. *J. Adv. Model. Earth Syst.*, **11 (12)**, 4395–4422.

Fu, H., and M. O'Neill, 2021b: A theory of spontaneous tropical cyclogenesis from quasi-random convection. *EarthArXiv*.

Fu, H., and M. O'Neill, 2021a: The role of random vorticity stretching in tropical depression genesis. *J. Atmos. Sci.*, **78 (12)**, 4143–4168.

Fuglestvedt, H. F., and J. O. Haerter, 2020: Cold pools as conveyor belts of moisture. *Geophys. Res. Lett.*, e2020GL087319.

Garg, P., S. W. Nesbitt, T. J. Lang, and G. Priftis, 2021: Diurnal cycle of tropical oceanic mesoscale cold pools. *J. Clim*, **34 (23)**, 9305–9326.

Gentine, P., A. Garelli, S.-B. Park, J. Nie, G. Torri, and Z. Kuang, 2016: Role of surface heat fluxes underneath cold pools. *Geophys. Res. Lett.*, **43 (2)**, 874–883.

Grandpeix, J.-Y., and J.-P. Lafore, 2010: A density current parameterization coupled with emanuel's convection scheme. part i: The models. *J. Atmos. Sci.*, **67 (4)**, 881–897.

Haerter, J. O., P. Berg, and C. Moseley, 2017: Precipitation onset as the temporal reference in convective self-organization. *Geophys. Res. Lett.*, **44 (12)**, 6450–6459.

Haerter, J. O., S. J. Böing, O. Henneberg, and S. B. Nissen, 2019: Circling in on convective organization. *Geophys. Res. Lett.*, **46 (12)**, 7024–7034.

Haerter, J. O., B. Meyer, and S. B. Nissen, 2020: Diurnal self-aggregation. *npj Climate and Atmospheric Science*, **3 (1)**, 1–11.

Hernandez-Duenas, G., L. M. Smith, and S. N. Stechmann, 2015: Stability and instability criteria for idealized precipitating hydrodynamics. *J. Atmos. Sci.*, **72 (6)**, 2379–2393.

Jeevanjee, N., and D. M. Romps, 2013: Convective self-aggregation, cold pools, and domain size. *Geophys. Res. Lett.*, **40 (5)**, 994–998.

Jeevanjee, N., and D. M. Romps, 2015: Effective buoyancy, inertial pressure, and the mechanical generation of boundary layer mass flux by cold pools. *J. Atmos. Sci.*, **72 (8)**, 3199–3213.

Jiménez, P. A., J. Dudhia, J. F. González-Rouco, J. Navarro, J. P. Montávez, and E. García-Bustamante, 2012: A revised scheme for the wrf surface layer formulation. *Monthly Weather Review*, **140 (3)**, 898–918.

Khairoutdinov, M. F., S. K. Krueger, C.-H. Moeng, P. A. Bogenschutz, and D. A. Randall, 2009: Large-eddy simulation of maritime deep tropical convection. *J. Adv. Model. Earth Syst.*, **1 (4)**.

Koren, I., and G. Feingold, 2011: Aerosol–cloud–precipitation system as a predator-prey problem. *Proc. Natl. Acad. Sci. U.S.A.*, **108 (30)**, 12 227–12 232.

Koren, I., E. Tziperman, and G. Feingold, 2017: Exploring the nonlinear cloud and rain equation. *Chaos*, **27 (1)**, 013 107.

Kuo, H., 1961: Convection in conditionally unstable atmosphere. *Tellus*, **13 (4)**, 441–459.

Langhans, W., and D. M. Romps, 2015: The origin of water vapor rings in tropical oceanic cold pools. *Geophys. Res. Lett.*, **42 (18)**, 7825–7834.

Langhans, W., K. Yeo, and D. M. Romps, 2015: Lagrangian investigation of the precipitation efficiency of convective clouds. *J. Atmos. Sci.*, **72 (3)**, 1045–1062.

Lee, J. H.-W., G. H. Jirka, and D. R. Harleman, 1974: Stability and mixing of a vertical round buoyant jet in shallow water. Tech. rep., MIT Energy Lab.

Lutsko, N. J., and T. W. Cronin, 2018: Increase in precipitation efficiency with surface warming in radiative-convective equilibrium. *J. Adv. Model. Earth Syst.*, **10 (11)**, 2992–3010.

Mapes, B. E., 1993: Gregarious tropical convection. *J. Atmos. Sci.*, **50 (13)**, 2026–2037.

Mapes, B. E., 1997: Equilibrium vs. activation control of large-scale variations of tropical deep convection. *The physics and parameterization of moist atmospheric convection*, Springer, 321–358.

Marshall, J., and R. A. Plumb, 2016: *Atmosphere, ocean and climate dynamics: an introductory text*. Academic Press.

Morrison, H., J. Curry, and V. Khvorostyanov, 2005: A new double-moment microphysics parameterization for application in cloud and climate models. part i: Description. *J. Atmos. Sci.*, **62 (6)**, 1665–1677.

Morrison, H., J. M. Peters, A. C. Varble, W. M. Hannah, and S. E. Giangrande, 2020: Thermal chains and entrainment in cumulus updrafts. part i: Theoretical description. *J. Atmos. Sci.*, **77 (11)**, 3637–3660.

Nissen, S. B., and J. O. Haerter, 2021: Circling in on convective self-aggregation. *Journal of Geophysical Research: Atmospheres*, **126 (20)**, e2021JD035 331.

Öktem, R., and D. M. Romps, 2021: Prediction for cloud spacing confirmed using stereo cameras. *J. Atmos. Sci.*, **78 (11)**, 3717–3725.

Parodi, A., and K. Emanuel, 2009: A theory for buoyancy and velocity scales in deep moist convection. *J. Atmos. Sci.*, **66 (11)**, 3449–3463.

Raymond, D. J., 1995: Regulation of moist convection over the west pacific warm pool. *J. Atmos. Sci.*, **52 (22)**, 3945–3959.

Rio, C., and Coauthors, 2013: Control of deep convection by sub-cloud lifting processes: the alp closure in the lmdz5b general circulation model. *Climate dynamics*, **40 (9)**, 2271–2292.

Romps, D. M., and A. B. Charn, 2015: Sticky thermals: Evidence for a dominant balance between buoyancy and drag in cloud updrafts. *J. Atmos. Sci.*, **72 (8)**, 2890–2901.

Romps, D. M., and N. Jeevanjee, 2016: On the sizes and lifetimes of cold pools. *Quart. J. Roy. Meteor. Soc.*, **142 (696)**, 1517–1527.

Romps, D. M., and Z. Kuang, 2010: Do undiluted convective plumes exist in the upper tropical troposphere? *J. Atmos. Sci.*, **67 (2)**, 468–484.

Romps, D. M., and R. Öktem, 2015: Stereo photogrammetry reveals substantial drag on cloud thermals. *Geophys. Res. Lett.*, **42 (12)**, 5051–5057.

Ross, A., A. M. Tompkins, and D. Parker, 2004: Simple models of the role of surface fluxes in convective cold pool evolution. *J. Atmos. Sci.*, **61 (13)**, 1582–1595.

Schlemmer, L., and C. Hohenegger, 2014: The formation of wider and deeper clouds as a result of cold-pool dynamics. *J. Atmos. Sci.*, **71 (8)**, 2842–2858.

Shaw, S. W., and P. Holmes, 1983: A periodically forced piecewise linear oscillator. *Journal of sound and vibration*, **90 (1)**, 129–155.

Thuburn, J., and G. A. Efstathiou, 2020: Marginal stability of the convective boundary layer. *J. Atmos. Sci.*, **77 (2)**, 435–442.

Tompkins, A. M., 2001: Organization of tropical convection in low vertical wind shears: The role of cold pools. *J. Atmos. Sci.*, **58 (13)**, 1650–1672.

Tompkins, A. M., and G. C. Craig, 1998: Time-scales of adjustment to radiative-convective equilibrium in the tropical atmosphere. *Quart. J. Roy. Meteor. Soc.*, **124 (552)**, 2693–2713.

Torri, G., and Z. Kuang, 2016: A lagrangian study of precipitation-driven downdrafts. *J. Atmos. Sci.*, **73 (2)**, 839–854.

Torri, G., and Z. Kuang, 2019: On cold pool collisions in tropical boundary layers. *Geophys. Res. Lett.*, **46 (1)**, 399–407.

Torri, G., Z. Kuang, and Y. Tian, 2015: Mechanisms for convection triggering by cold pools. *Geophys. Res. Lett.*, **42 (6)**, 1943–1950.

Turner, J., 1986: Turbulent entrainment: the development of the entrainment assumption, and its application to geophysical flows. *J. Fluid Mech.*, **173**, 431–471.

Ungarish, M., 2009: *An introduction to gravity currents and intrusions*. CRC press.

Wing, A. A., K. Emanuel, C. E. Holloway, and C. Muller, 2017: Convective self-aggregation in numerical simulations: A review. *Shallow clouds, water vapor, circulation, and climate sensitivity*, 1–25.

Yang, Q., L. R. Leung, Z. Feng, F. Song, and X. Chen, 2021: A simple lagrangian parcel model for the initiation of summertime mesoscale convective systems over the central united states. *J. Atmos. Sci.*, **78 (11)**, 3537–3558.